

# GLoW: novel methods for wave-optics phenomena in gravitational lensing

Hector Villarrubia-Rojo,<sup>1,2,\*</sup> Stefano Savastano,<sup>2,†</sup> Miguel Zumalacárregui,<sup>2,‡</sup>  
Lyla Choi,<sup>3,§</sup> Srashti Goyal,<sup>2,¶</sup> Liang Dai,<sup>4</sup> and Giovanni Tambalo<sup>5,\*\*</sup>

<sup>1</sup>*Departamento de Física Teórica, Universidad Complutense de Madrid, 28040 Madrid, Spain*

<sup>2</sup>*Max Planck Institute for Gravitational Physics (Albert Einstein Institute)  
Am Mühlenberg 1, D-14476 Potsdam-Golm, Germany*

<sup>3</sup>*Department of Physics, Princeton University, Princeton, NJ 08544*

<sup>4</sup>*University of California at Berkeley, Berkeley, California 94720, USA*

<sup>5</sup>*Institut für Theoretische Physik, ETH Zürich, 8093 Zürich, Switzerland*

(Dated: September 10, 2024)

Wave-optics phenomena in gravitational lensing occur when the signal’s wavelength is commensurate to the gravitational radius of the lens. Although potentially detectable in lensed gravitational waves, fast radio bursts and pulsars, accurate numerical predictions are challenging to compute. Here we present novel methods for wave-optics lensing that allow the treatment of general lenses. In addition to a general algorithm, specialized methods optimize symmetric lenses (arbitrary number of images) and generic lenses in the single-image regime. We also develop approximations for simple lenses (point-like and singular isothermal sphere) that drastically outperform known solutions without compromising accuracy. These algorithms are implemented in *Gravitational Lensing of Waves* (GLoW): an accurate, flexible, and fast code. GLoW efficiently computes the frequency-dependent amplification factor for generic lens models and arbitrary impact parameters in  $\mathcal{O}(1\text{ ms})$  to  $\mathcal{O}(10\text{ ms})$  depending on the lens configuration and complexity. GLoW is readily applicable to model lensing diffraction on gravitational-wave signals, offering new means to investigate the distribution of dark-matter and large-scale structure with signals from ground and space detectors.

## CONTENTS

I. Introduction	1
II. Lensing formalism	3
III. Time domain	4
A. Contour method	4
B. Integral for symmetric lenses	4
C. Grid method	6
IV. Frequency domain	6
A. Regularization	6
B. FFT with varying resolution	7
C. Direct Fourier integral	7
V. Analytical results	8
A. Point lens	8
B. Singular isothermal sphere	9
VI. Code structure and performance	10
A. Outline	10
B. Time domain	11
C. Frequency domain	12
D. Performance and precision	12

VII. Conclusions	12
Acknowledgments	13
A. Lens catalog	15
1. Point lens (PL)	15
2. Singular Isothermal Sphere (SIS)	15
3. Cored isothermal sphere (CIS)	15
4. Truncated singular isothermal sphere (tSIS)	15
5. Elliptical Singular Isothermal Sphere (eSIS)	16
6. Navarro-Frenk-White (NFW)	16
7. External Shear and Convergence	16
B. Regularization scheme	16
C. Code precision	18
References	20

## I. INTRODUCTION

Like a magnifying glass, gravitational fields deflect and focus signals propagating through the universe, in some cases producing multiple images of the same source [1]. This broad set of phenomena, collectively denoted *gravitational lensing*, is essential to interpret many astronomical observations correctly. In addition, observation of lensing effects has led to many applications in cosmology and astrophysics, which include finding extra-solar planetary systems [2, 3], directly imaging supermassive black holes [4, 5], mapping the distribution of dark matter [6–8], measuring the Universe’s expansion [9] and testing gravity [10, 11].

\* hectorvi@ucm.es

† stefano.savastano@aei.mpg.de

‡ miguel.zumalacarregui@aei.mpg.de

§ lc3535@princeton.edu

¶ srashti.goyal@aei.mpg.de

\*\* gtambalo@phys.ethz.ch

In most applications, gravitational lensing can be understood as signals propagating over well-defined trajectories, denoted rays [12]. Rays define the image positions, their magnifications, relative arrival times, and apparent deformation of a source. This description, known as *geometric optics* (GO), emerges through Fermat’s principle, stating that light travels between two points along the path that requires the least time. Geometric optics is valid for signals with wavelengths much smaller than the difference in path length. This is satisfied in all electromagnetic lensing phenomena observed so far, due to the large hierarchy between typical astronomical objects and the radiation able to penetrate the Earth’s atmosphere.

The *wave optics* regime describes the propagation of signals with arbitrarily low frequencies, where geometric optics fails. The primary effect observed in this regime is *diffraction*, the wavefront distortion caused by obstacles during propagation. Diffraction is responsible for frequency-dependent effects on the signal. It is well-known in optics, where diffraction patterns have found many applications, e.g. to characterize materials (crystallography), but these uses rely on light-matter interactions. Gravitational diffraction of electromagnetic signals can be caused by extremely light objects. Although it has not yet been observed, electromagnetic lensing diffraction could be used to probe planet-scale objects and compact dark-matter objects [13–16].

Gravitational waves (GWs) offer a promising observational window for wave-optic lensing phenomena [17]. Phase coherence of GWs prevents the blurring of diffraction patterns expected in extended sources, and ab initio emission models can help discern frequency-dependent distortions of the signal. Typical GW wavelengths are orders of magnitude larger than radio waves that can penetrate the atmosphere, making diffraction by typical lenses observable. GWs in ground-based detectors ( $\sim 100$  Hz) are sensitive to diffraction from objects with  $1 - 10^3 M_\odot$  (solar masses) [18], including optically thick stellar populations in galaxies producing strong lensing [19–21]. Detectors at lower frequencies can probe much heavier structures: space detectors like LISA (mHz) can probe halos/subhalos with  $10^5 - 10^8 M_\odot$  [22, 23] and pulsar-timing arrays (nHz) can probe wave-optics by galactic-scale objects  $\sim 10^{12} M_\odot$  [24]. The prospect of detection and potential applications requires the development of new tools to explore wave-optics lensing phenomena [25, Sec. 11.2].


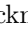
Accurately computing wave-optics lensing predictions is numerically challenging. General predictions require conditionally convergent integrals of rapidly oscillating functions over the lens plane. Previous studies have used direct integration [26, 27], Levin’s method [28, 29], sampling the Fermat potential over isochrone lines [13, 20, 30], by discretizing the lens plane [19, 31, 32], by direct fast-fourier transform convolution [33], or using analytic continuation (Picard-Lefschetz) theory [34, 35]. Analytical expressions exist only for the isolated point lens [36] and series expansions have been developed for a few sym-

metric lenses [37, 38], but even these solutions become costly to evaluate at high frequency  $\times$  lens mass. Waveforms for high-mass lensing objects could allow us especially to probe the large-scale structure of the universe using LISA [22, 23, 39–41].

Several publicly available packages have been developed for GW lensing. `LensingGW`<sup>1</sup> [42] is restricted to GO, and thus large lens masses. `GRAVELAMPS`<sup>2</sup> [38] uses a combination of numerical integration and series expansion for symmetric lenses. `Glworia`<sup>3</sup> [30] employs contour integration to compute amplification factors for symmetric lenses. However, these codes are not yet fast enough for sampling over large sets of parameters: applications to parameter estimation require pre-computing and interpolating the lensing diffraction effects. Dense distributions of stars embedded in galactic-scale lenses have been analyzed, but all analyses have relied on private codes [19–21, 31, 43–45].

In this work, we present a series of fast and accurate algorithms to compute wave-optics lensing diffraction and their implementation into *Gravitational Lensing of Waves* (GLOW), a flexible and modular software package in Python & C. The key features of the package are:

- Wave-optics lensing methods for general lenses and configurations.
- Optimized algorithms for both symmetric lenses and the single-image regime.
- Bespoke treatment of singular contributions and lens-plane asymptotics.
- Multiple efficient methods for Fourier transform.
- A catalog of commonly used lens profiles and flexibility to add any arbitrary lens to the code.
- A fast and accurate implementation of the point lens and the singular isothermal sphere.
- Tunable precision parameters to control accuracy and speed.
- Computation of lensed waveforms, in the time and frequency domains.

GLOW is publicly available <sup>4</sup>, for updated details see the documentation <sup>5</sup>. Please acknowledge its use by citing this paper. The scripts used to generate the figures in this paper are also available in the public repository. We point the reader to Refs. [23, 41, 46] for some of the GW lensing science case studies that have been enabled by GLOW.

<sup>1</sup> <https://gitlab.com/gpagano/lensinggw>

<sup>2</sup> <https://git.ligo.org/mick.wright/Gravelamps>

<sup>3</sup> <https://github.com/mhycheung/glworia>

<sup>4</sup> [https://github.com/miguelzuma/GLOW\\_public](https://github.com/miguelzuma/GLOW_public)

<sup>5</sup> [https://miguelzuma.github.io/GLOW\\_public/index.html](https://miguelzuma.github.io/GLOW_public/index.html)

The rest of this article is organised as follows, Sec. II introduces the concepts and equations involved in gravitational lensing computations in the wave-optics regime. Sec. III describes the algorithms used for the time-domain computation, Sec. IV describes the regularization and conversion to the frequency domain. Sec. V presents efficient analytical results in some symmetric lenses. Sec. VI presents the structure of the code and discusses its performance. We provide our conclusions in Sec. VII. The appendices present a catalogue of implemented lenses (A), expressions for the regularization functions (B), and tests of GLoW's precision (C).

## II. LENSING FORMALISM

In this Section we will describe the basic setup of gravitational lensing [1] and notation followed by the code. We work in units where  $c = 1$ .

The lensing of gravitational waves is characterized by the *amplification factor*  $F(f)$  multiplying an unlensed strain  $\tilde{h}_0$  in the frequency domain as follows:

$$F(f) \equiv \frac{\tilde{h}(f)}{\tilde{h}_0(f)}. \quad (1)$$

Here,  $\tilde{h}_0(f)$  and  $\tilde{h}(f)$  are Fourier transforms of the unlensed and lensed strains respectively. For a lens located at redshift  $z_L$ , the distance  $D_{LS}$  between the lens and the source is

$$D_{LS} = D_S - \frac{1 + z_L}{1 + z_S} D_L, \quad (2)$$

where  $D_S$  and  $D_L$  are the angular diameter distances to the source and the lens respectively. We can then define an effective distance

$$d_{\text{eff}} \equiv \frac{D_L D_{LS}}{(1 + z_L) D_S}. \quad (3)$$

For positions on the lens plane  $\boldsymbol{\xi}$  and on the source plane  $\boldsymbol{\eta}$ , we define the dimensionless parameters

$$\mathbf{x} = \frac{\boldsymbol{\xi}}{\xi_0}, \quad \mathbf{y} = \frac{D_L}{\xi_0 D_S} \boldsymbol{\eta}. \quad (4)$$

Here,  $\mathbf{y}$  is known as the *impact parameter* and  $\xi_0$  is a dimensionful (but otherwise arbitrary) scale, typically chosen depending on the lens. See Appendix A for more details on the choice of  $\xi_0$ .

For a given density profile  $\rho(\mathbf{r})$  of a lens, the projected mass density is obtained by integrating in the  $z$ -direction perpendicular to the lens plane:

$$\Sigma(\boldsymbol{\xi}) = \int_{-\infty}^{\infty} dz \rho(\boldsymbol{\xi}, z). \quad (5)$$

The lensing potential  $\psi(\mathbf{x})$  for the particular lens is then found by solving

$$\nabla_{\mathbf{x}}^2 \psi(\mathbf{x}) = 2\kappa(\mathbf{x}), \quad (6)$$

where the *convergence*  $\kappa$  is given by

$$\kappa(\mathbf{x}) = \frac{\Sigma(\xi_0 \mathbf{x})}{\Sigma_{\text{cr}}}, \quad (7)$$

and the *critical density*  $\Sigma_{\text{cr}}$  is

$$\Sigma_{\text{cr}} = \frac{1}{4\pi G(1 + z_L)d_{\text{eff}}}. \quad (8)$$

Here,  $G$  is Newton's constant. We can solve (6) for the lensing potential using the 2D Green's function

$$\psi(\mathbf{x}) = \frac{1}{\pi} \int d^2 x' \kappa(\mathbf{x}') \log |\mathbf{x} - \mathbf{x}'|. \quad (9)$$

The lensing potential is then incorporated into the amplification factor via the *Fermat potential*, which is defined as

$$\phi(\mathbf{x}, y) = \frac{1}{2} |\mathbf{x} - \mathbf{y}|^2 - \psi(\mathbf{x}) \quad (10)$$

$$= \frac{1}{2} (x_1^2 + x_2^2 + y^2) - x_1 y - \psi(x_1, x_2), \quad (11)$$

$$\tilde{\phi} \equiv \phi - t_{\text{min}}, \quad (12)$$

where  $t_{\text{min}}$  is the minimum of the Fermat potential, such that  $\tilde{\phi}(\mathbf{x}_{\text{min}}) = 0$ . We also choose the orientation of the axes such that the  $x_1$  axis is aligned with the impact parameter  $\mathbf{y}$ . The amplification factor (1) is defined in terms of the Fermat potential as

$$F(w) = \frac{w}{2\pi i} \int d^2 x \exp(iw \tilde{\phi}(\mathbf{x}, y)). \quad (13)$$

Here we introduced the *dimensionless frequency*

$$w \equiv 8\pi G M_{Lz} f, \quad (14)$$

where  $M_{Lz}$  is the redshifted *effective lens mass*

$$M_{Lz} \equiv \frac{\xi_0^2}{4G d_{\text{eff}}}. \quad (15)$$

Defining the Fourier transform as

$$\mathcal{F}[f(x)] \equiv \int_{-\infty}^{\infty} dx e^{-iwx} f(x), \quad (16)$$

the time-domain version of the amplification factor can be written as

$$F(w) = \frac{w}{2\pi i} \int_{-\infty}^{\infty} d\tau e^{i w \tau} I(\tau) = \frac{w}{2\pi i} \mathcal{F}^*[I(\tau)], \quad (17)$$

$$I(\tau) = \int d^2 x \delta(\tilde{\phi}(\mathbf{x}) - \tau), \quad (18)$$

where  $*$  denotes complex conjugation. In many cases, we will use the notation

$$I(t) \equiv \int d^2 x \delta(\phi(\mathbf{x}) - t), \quad (19)$$

where  $t \equiv \tau + t_{\text{min}}$ . The conversion to physical time and frequency is

$$t_{\text{phys}} = \frac{\xi_0^2}{d_{\text{eff}}} t = 4GM_{Lz} t, \quad (20a)$$

$$f = \frac{1}{2\pi} \frac{d_{\text{eff}}}{\xi_0^2} w = \frac{w}{8\pi GM_{Lz}}. \quad (20b)$$

### III. TIME DOMAIN

In this Section, we provide an overview of the algorithms used to compute the time-domain version of the amplification factor  $I(\tau)$ .

#### A. Contour method

The original proposal of computing  $I(\tau)$  as a contour integral dates back to the work of Ulmer and Goodman in 1994 [13]. Since then, several works have applied this method [41, 47–49]. We will assume for now that there is a single image, i.e. the global minimum. We can change from Cartesian to polar coordinates centered at this minimum

$$x_1 = x_1^0 + R \cos \theta , \quad (21)$$

$$x_2 = x_2^0 + R \sin \theta , \quad (22)$$

such that  $\phi(x_1^0, x_2^0) = t_{\min}$ . With this change of coordinates, the time-domain integral can be rewritten as

$$I(t) = \int R dR d\theta \delta(\phi(R, \theta) - t) . \quad (23)$$

If  $\partial_R \phi \neq 0$ , we can invert

$$\phi(R, \theta) = t , \quad (24)$$

to obtain  $R(\theta, t)$ . We can then solve the integral over the  $\delta$  function, plugging in this solution

$$I(t) = \int_0^{2\pi} \frac{R(\theta, t)}{|\partial_R \phi|} d\theta . \quad (25)$$

Finally, the system of differential equations that must be solved to find both the curve  $R(\theta, t)$  and  $I(t)$  is

$$\frac{dI}{d\theta} = \frac{R}{|\partial_R \phi|} , \quad (26)$$

$$\frac{dR}{d\theta} = -\frac{\partial_\theta \phi}{\partial_R \phi} . \quad (27)$$

Since we are just interested in  $I(t)$ , we can integrate this system from  $\theta = 0$  to  $2\pi$ , with initial conditions  $I(\theta = 0, t) = 0$  and  $R(\theta = 0, t)$  such that  $\phi(R(0, t), 0) = t$ . The previous condition  $\partial_R \phi \neq 0$  can be violated when the lensing effects are very aggressive and the contours are very deformed. In this case, we must find a parametric representation of the constant time-delay curve as  $R(\sigma, t)$ ,  $\theta(\sigma, t)$ . We will choose the parameterization

$$\frac{dR}{d\sigma} = -\partial_\theta \phi , \quad \frac{d\theta}{d\sigma} = \partial_R \phi , \quad (28)$$

that transforms the integral into

$$I(t) = \oint R(\sigma, t) d\sigma . \quad (29)$$

The problem is then equivalent to solving the following system of differential equations

$$\frac{dI}{d\sigma} = R , \quad (30a)$$

$$\frac{dR}{d\sigma} = -\partial_\theta \phi , \quad (30b)$$

$$\frac{d\theta}{d\sigma} = \partial_R \phi . \quad (30c)$$

This time, we must integrate from  $\sigma = 0$  until we close the curve, i.e.  $\theta(\sigma_f, t) = 2\pi$  and  $R(\sigma_f, t) = R(0, t)$ . The initial conditions are chosen as before. The method can be generalized from the single-image case that we have developed here to a generic strong-lensing scenario. It can be summarized as follows:

1. Find all the critical points solving the lens equation  $\nabla \phi = 0$ .
2. Some lenses also present special points, like singularities and cusps. These points may introduce discontinuities and divergences in  $\nabla \phi$ . However, if we use a regularized version of the lens these points reduce to a standard critical point, so in the following discussion we will also refer to them collectively as “critical points”.
3. Once we have found all the critical points we can divide the lens plane into regions covered by different families of contours. The regions are separated by critical curves, which are curves of constant time delay that cross a saddle point.
4. Each of these families of contours starts at a critical point with time delay  $t_0^i$  and dies at another critical point  $t_f^i$ . These contours then contribute to  $I(t)$  in the range  $[t_0^i, t_f^i]$ . In each of these regions we can choose coordinates (21), with  $\mathbf{x}^0$  being the critical point at the center of the contours, and integrate the system (30) to obtain the contribution to  $I(t)$ .
5. Finally, once we have identified all the families of contours and their contributions, we can add them to find the total  $I(t)$ .

Notice that, after finding the regions in the lens plane, the integration over each contour is independent, so the algorithm can be trivially parallelized. A non-trivial example of this method is shown in Fig. 1.

#### B. Integral for symmetric lenses

In the axisymmetric case, i.e.  $\psi(\mathbf{x}) = \psi(x)$ , it is possible to reduce the problem in the time domain to the computation of an ordinary integral in one variable. First, we must choose coordinates adapted to the symmetry of the lensing potential

$$x_1 = r \cos \varphi , \quad (31a)$$

$$x_2 = r \sin \varphi . \quad (31b)$$

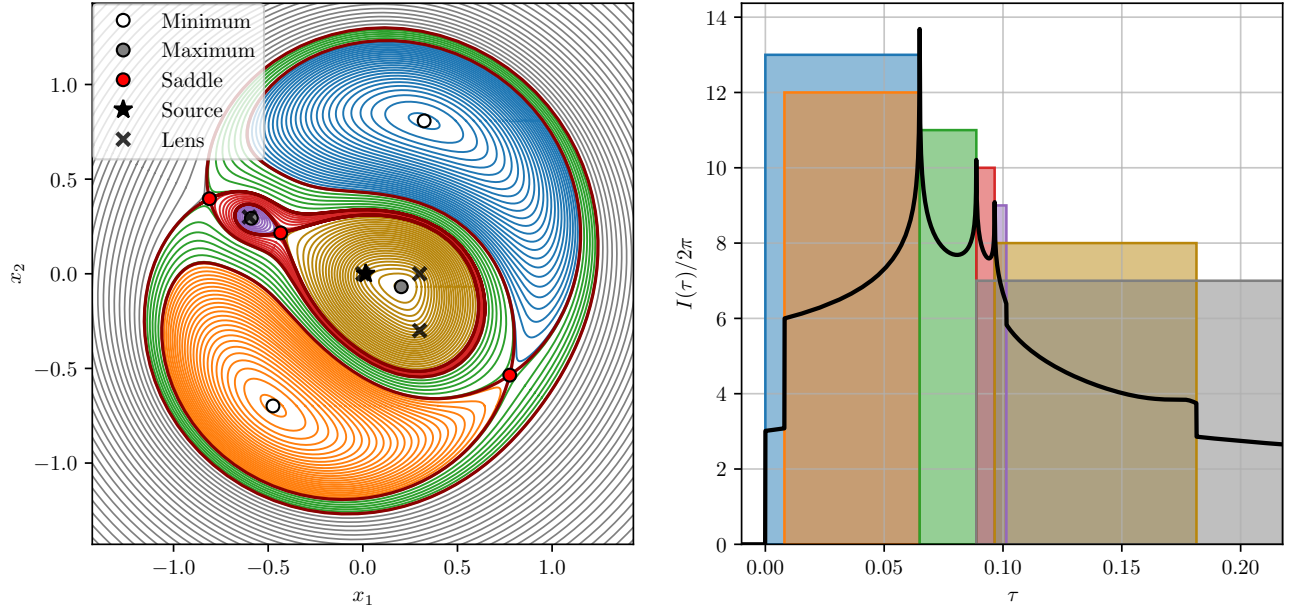


FIG. 1. Non-trivial application of the contour method in Sec. III A. The lens is composed of four CISs (see App. A for the definition). **Left:** Equal time delay contours and critical points of the Fermat potential. Each family of contours starts and ends at a critical point, and is represented with a different color. The outermost family of contours extends to infinity. **Right:** Each contour, with time delay  $\tau$ , contributes to a point in  $I(\tau)$ . The range where each family contributes is represented with colored boxes. The boxes are displayed with different heights to aid visualization.

Defining  $z \equiv \cos \varphi$ , we can rewrite (19) as

$$\phi(r, z) = \frac{1}{2}(r^2 + y^2) - yrz - \psi(r), \quad (32)$$

$$I(t) = \int_{-1}^1 \frac{dz}{\sqrt{1-z^2}} \int_0^\infty r dr \delta(\phi(r, z) - t). \quad (33)$$

Solving the integral over  $z$  we get

$$I(t) = \int_0^\infty \frac{2dr}{y\sqrt{1-z_*^2}} \Theta(1-z_*^2),$$

$$z_* \equiv \frac{1}{2yr} (r^2 - 2\psi(r) - t), \quad (34)$$

where  $\Theta$  is the Heaviside step function. The computation can be simplified further if we split the integrand into the regions where it is non-zero, i.e.  $r \in (r_{\min}, r_{\max}) \rightarrow |z_*| < 1$ ,

$$I(t) = \sum_i \int_{r_{\min}^i}^{r_{\max}^i} \alpha(r) dr, \quad (35)$$

$$\alpha(r) \equiv \frac{2r}{\sqrt{-\phi_+ \phi_-}}, \quad (36)$$

$$\phi_\pm \equiv \frac{1}{2}r^2 + \frac{1}{2}y^2 - \psi(r) - t \mp ry. \quad (37)$$

At the limits  $r_{\max}$  and  $r_{\min}$  we have  $\phi_+ \phi_- = 0$ , so even though the function is integrable, it can be hard to compute numerically. We make one more change of variables

that smooths the integrand

$$\zeta = \begin{cases} \sqrt{\frac{r - r_{\min}}{r_{\text{mid}} - r_{\min}}}, & r \in (r_{\min}, r_{\text{mid}}) \\ \sqrt{\frac{r_{\max} - r}{r_{\max} - r_{\text{mid}}}}, & r \in (r_{\text{mid}}, r_{\max}) \end{cases} \quad (38)$$

where  $r_{\text{mid}} \equiv (r_{\max} + r_{\min})/2$ . Using this new variable we just need to compute a single integral

$$I(t) = 2 \int_0^1 \zeta d\zeta \sum_i \sqrt{\Delta^i} \left\{ \alpha(r_{\max}^i - \Delta^i \zeta^2) + \alpha(r_{\min}^i + \Delta^i \zeta^2) \right\}, \quad (39)$$

with  $\Delta^i \equiv (r_{\max}^i - r_{\min}^i)/2$ . The whole algorithm can be summarized as follows:

1. Find all the critical points (and special points, see Sec. III A). In the axisymmetric case, all the critical points lie in the  $x_1$  line (i.e.  $x_2 = 0$ ) so now we just need to deal with a much simpler 1D root-finding problem.
2. For each  $t$ , determine the regions where  $\phi_+(r)\phi_-(r) < 0$  (37) by finding the values  $(r_{\min}^i, r_{\max}^i)$  where  $\phi_+ \phi_- = 0$ .
3. Perform the integral (39), summing over all the  $i$  regions where  $\phi_+ \phi_- < 0$ .



### C. Grid method

Finally, another way to solve the time-domain integral, first proposed in [19], is to compute it directly as a surface integral. This method has been applied in a number of works [31, 43, 50, 51]. Starting again with the time-domain version of the amplification factor

$$I(t) = \int d^2x \delta(\phi(\mathbf{x}) - t), \quad (40)$$

the simplest approach we can follow to compute this integral is to represent the delta function as

$$\delta_n(x) = \begin{cases} 0, & x < -1/2n \\ n, & -1/2n < x < 1/2n \\ 0, & x > 1/2n \end{cases} \quad (41)$$

when  $n \rightarrow \infty$ . In this way, we obtain a discrete representation

$$I(t) \simeq I_i, \quad \text{for } t \in [t_i - \Delta t_i/2, t_i + \Delta t_i/2], \quad (42)$$

that converges to the real result as we reduce the size of the boxes  $\Delta t_i$ . The approach we follow to implement this method is the following:

1. Find the global minimum of the Fermat potential,  $t_{\min}$ .
2. Create a temporal grid from  $t_{\min}$  to a given  $t_{\max}$ , logarithmically spaced.
3. Define a spatial grid and evaluate  $\phi(\mathbf{x})$  on this grid.
4. Build the discrete representation  $I_i$  as a histogram.

## IV. FREQUENCY DOMAIN

Having computed the time-domain integral  $I(\tau)$ , in this Section, we detail the regularization and Fourier transform procedures we follow to transform  $I(\tau)$  into the frequency domain.

### A. Regularization

Once the time-domain integral has been computed, we must compute its Fourier transform (FT) to obtain the amplification factor

$$F(w) = \frac{w}{2\pi i} \int_{-\infty}^{\infty} d\tau e^{iw\tau} I(\tau) = \frac{w}{2\pi i} \mathcal{F}^*[I(\tau)]. \quad (43)$$

However, the presence of discontinuities and singularities in  $I(\tau)$  makes this seemingly-simple operation much more complicated in practice. In [47], a regularization approach was proposed to overcome this problem. The

main idea is to split the result into a regular and singular part,

$$I(\tau) = I_{\text{reg}}(\tau) + I_{\text{sing}}(\tau), \quad (44a)$$

$$F(w) = F_{\text{reg}}(w) + F_{\text{sing}}(w), \quad (44b)$$

such that  $I_{\text{sing}}$  is an analytical expression that we can Fourier transform analytically (i.e.  $F_{\text{sing}}$  is also known) and  $I_{\text{reg}}$  is easier to Fourier transform numerically. The regularization scheme proposed in [47] was to add for each minimum (type I image)

$$I_{\text{sing}}^m(\tau) \equiv 2\pi\sqrt{\mu_j} \Theta(\tau - \tau_j), \quad (45a)$$

$$F_{\text{sing}}^m(w) = \sqrt{\mu_j} e^{iw\tau_j}, \quad (45b)$$

for each maximum (type II image)

$$I_{\text{sing}}^M(\tau) \equiv 2\pi\sqrt{\mu_j} \Theta(\tau_j - \tau), \quad (46a)$$

$$F_{\text{sing}}^M(w) = -\sqrt{\mu_j} e^{iw\tau_j}, \quad (46b)$$

and for each saddle point (type III image)

$$I_{\text{sing}}^s(\tau) \equiv -2\sqrt{\mu_j} e^{-|\tau - \tau_j|/T} \log|\tau - \tau_j|, \quad (47a)$$

$$F_{\text{sing}}^s(w) = \frac{2iw}{\pi} \sqrt{\mu_j} e^{iw\tau_j} \Re(\mathcal{I}), \quad (47b)$$

$$\begin{aligned} \mathcal{I} &\equiv \int_0^{\infty} dt \log(t) e^{-t/T + iw t} \\ &= -\frac{\gamma_E + \log(T^{-1} - iw)}{T^{-1} - iw}, \end{aligned} \quad (47c)$$

where  $T$  is a free parameter.

This scheme removes all the discontinuities and singularities associated with the geometric optics result, typically reducing the error in the FT at high frequencies. This regularization has the clear advantage of being very easy to evaluate in terms of elementary functions but also presents some drawbacks, e.g.  $I_{\text{reg}}(\tau)$  is not zero for  $\tau < 0$  and  $I_{\text{sing}}(\tau)$  contains free parameters.

The most important problem, however, is the presence of errors in the FT at low frequencies. These arise from the high- $\tau$  behaviour of  $I(\tau)$ , usually a power-law tail. The new regularization scheme that we propose in this work can handle both the geometric-optics singularities and these long tails, at the cost of introducing more complex regularizing functions. We find that, numerically, the tradeoff of reducing the complexity of the FT while increasing the cost of computing  $I_{\text{sing}}$  and  $F_{\text{sing}}$  is highly beneficial.

We will assume that the asymptotic behaviour of  $I(\tau)$  is

$$\frac{I(\tau \rightarrow \infty)}{2\pi} \sim 1 + \frac{I_{\text{asympt}}}{\tau^\sigma}, \quad (48)$$

and define

$$C_M \equiv \sum_{\text{max}} \sqrt{|\mu_j|}, \quad C_m \equiv \sum_{\text{loc min}} \sqrt{|\mu_j|}, \quad (49)$$

where the second sum spans only the local minima, and we will also denote as  $\sqrt{|\mu_{\min}|}$  the magnification of the global minimum. With these definitions we can write the singular contribution

$$\begin{aligned} \frac{I_{\text{sing}}(\tau)}{2\pi} &= \sum_{\text{loc min}} \sqrt{|\mu_j|} \Theta(\tau - \tau_j) + \sum_{\text{max}} \sqrt{|\mu_j|} \Theta(\tau_j - \tau) \\ &\quad - \mathcal{C}_M + (1 - \mathcal{C}_m + \mathcal{C}_M) \Theta(\tau) \\ &\quad + R_0 \left( \sqrt{|\mu_{\min}|} - 1 - \mathcal{C}_M + \mathcal{C}_m, I_{\text{asyp}}, \sigma; \tau \right) \\ &\quad + \sum_{\text{saddle}} S_{\text{full}} \left( \frac{2\sqrt{|\mu_j|}}{\pi\tau_j}, \tau_j; \tau \right), \end{aligned} \quad (50)$$

and its Fourier counterpart as

$$\begin{aligned} F_{\text{sing}}(w) &= \sum_{\text{loc min}} \sqrt{|\mu_j|} e^{iw\tau_j} - \sum_{\text{max}} \sqrt{|\mu_j|} e^{iw\tau_j} \\ &\quad + 1 - \mathcal{C}_m + \mathcal{C}_M \\ &\quad + \tilde{R}_0 \left( \sqrt{|\mu_{\min}|} - 1 - \mathcal{C}_M + \mathcal{C}_m, I_{\text{asyp}}, \sigma; w \right) \\ &\quad + \sum_{\text{saddle}} \tilde{S}_{\text{full}} \left( \frac{2\sqrt{|\mu_j|}}{\pi\tau_j}, \tau_j; w \right). \end{aligned} \quad (51)$$

The regularizing functions are lengthy and are collected in Appendix B.

## B. FFT with varying resolution

Choosing the right regularization scheme is an important ingredient to correctly transform  $I(\tau)$  to the frequency domain, but not the only one. The fastest way to perform the Fourier transform is to use the Fast Fourier Transform (FFT), but a naive implementation will face several obstacles:

- For typical applications to GW lensing, we will need to compute the amplification factor for frequencies spanning several orders of magnitude. Since the FFT samples the functions linearly, key features at low frequency (e.g. Fig. 2), will be severely undersampled. The simplest way to overcome this limitation is to extend the Fourier transform to higher frequencies than are actually needed, increasing then the number of points and effectively improving the sampling at low  $w$ . This of course has a significant impact on the performance.
- Even if we do not need denser sampling at lower frequencies, another common problem is the appearance of errors both at high and low frequencies. This can again be mitigated by performing an FFT over a wider range than is actually needed, improving the overall sampling in the time domain. The downside again is a loss of performance.

- Finally, even after computing a larger (slower) FFT, there is another difficulty that will slow down the computation. The typical strategy to lens a waveform is to precompute  $F(w)$  with an FFT and then interpolate it as needed over the waveform frequencies. If we compute a very large FFT, to correctly sample the lower frequencies, we will oversample the high frequencies, ending up with a grid much larger than actually needed and much slower to interpolate.

In order to overcome these problems, we generalized a method already considered in [47] and [48]. The main idea is to construct  $F(w)$  out of several small FFTs rather than a single, big one. In this way, we sample  $I(\tau)$  with varying resolution and then we assemble all the contributions. If we want to compute  $F(w)$  between two frequencies  $w_{\min}$  and  $w_{\max}$ , we start by dividing  $w$  into logarithmically-spaced frequency ranges  $[w^i, 2^N w^i]$ , where  $N$  is a constant and  $w^{i+1} = 2^N w^i$ . We then perform independent FFTs in each of this ranges, following the same strategy as for the naive FFT: we compute a larger FFT than actually needed and discard the low and high frequency range when the errors start creeping in. Finally, we piece all the contributions together.

This procedure overcomes all the problems outlined before. First, it samples more uniformly the amplification factor, without incurring any penalty for going to higher or lower frequencies. Secondly, the performance is much better, since it is much faster to perform several small FFTs rather than a large one. Finally, since the grid is more sparse, the interpolation is also faster. The precision achieved with this method is also very good, as shown in Figs. 8 and 9.

## C. Direct Fourier integral

The FFT method should always be preferred for applications requiring high speed, since it can compute  $F(w)$  automatically over a grid extremely quickly. However, we also wanted to provide an alternative method to cross-check the previous scheme.

This second approach is only limited by the finite sampling of  $I(\tau)$  (and numerical errors) and can then be easily improved and tested. The main idea is that, since in most applications we will precompute  $I(\tau)$  on a grid and linearly interpolate it, the Fourier transform can be computed exactly as a sum.

If we represent  $I(\tau)$  with a linear-interpolation approximation

$$I(\tau) = \begin{cases} I(\tau=0) + \frac{\tau}{\tau_0} (I(\tau=0) - I_0), & \tau \in [0, \tau_0) \\ I_i + \frac{\tau - \tau_i}{\tau_{i+1} - \tau_i} (I_{i+1} - I_i), & \tau \in [\tau_i, \tau_{i+1}) \\ 0, & \tau \in [\tau_{N-1}, \infty) \end{cases} \quad (52)$$

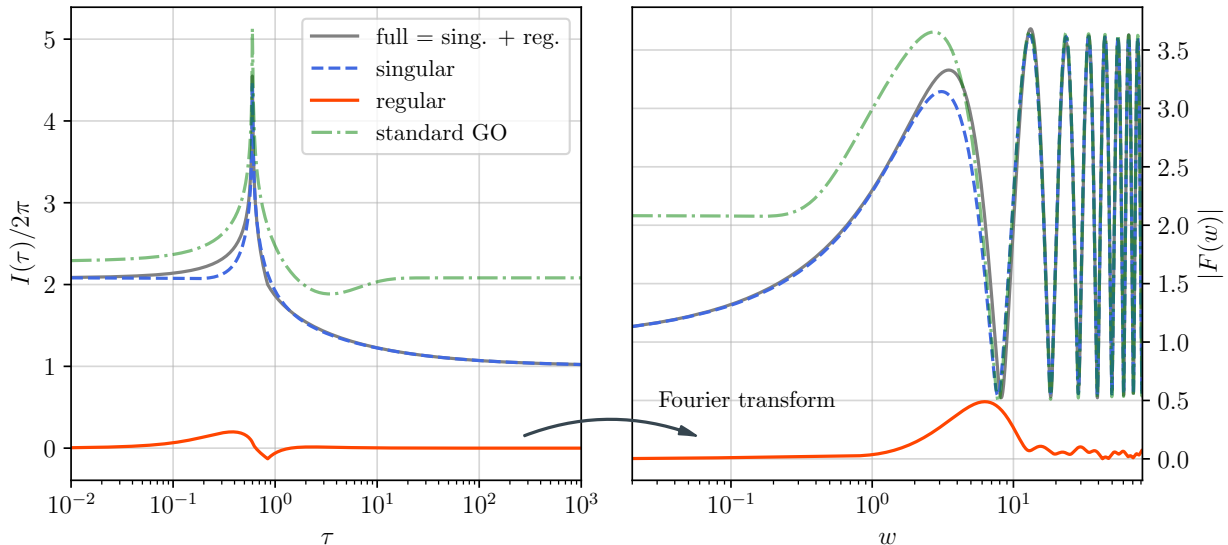


FIG. 2. Outline of our regularization procedure. **Left:** We start by computing the time domain integral, using any of the methods in Sec. III. We then regularize it, subtracting the analytical singular contribution (50). This regularization scheme subtracts the saddle point divergence, the step function at  $\tau = 0$ , as well as the slowly decaying tail at large  $\tau$ . **Right:** The regular part is then Fourier transformed, using any of the methods in Sec. IV. Finally, we recover the full amplification factor adding back (51), i.e. the (analytical) Fourier transform of the singular contribution. For comparison, we also show the old regularization scheme, standard GO, representing only the singular contribution given by Eqs. (45)-(47).

we can compute the amplification factor analytically and express it as

$$F(w) = \sum_{i=-1}^{N-2} J_i \left\{ \left( I_{i+1} + \frac{i}{w} \frac{\Delta I_i}{\Delta \tau_i} \right) (1 - D_i) - \Delta I_i \right\}, \quad (53)$$

where

$$\Delta I_i = I_{i+1} - I_i, \quad \Delta I_{-1} = I_0 - I(\tau = 0), \quad (54a)$$

$$\Delta \tau_i = \tau_{i+1} - \tau_i, \quad \Delta \tau_{-1} = \tau_0, \quad (54b)$$

$$D_i = e^{i w \Delta \tau_i}, \quad D_{-1} = e^{i w \Delta \tau_{-1}}, \quad (54c)$$

$$J_i = J_{i-1} D_{i-1}, \quad J_{-1} = \frac{1}{2\pi}. \quad (54d)$$

The main drawback of this method is that each frequency must be computed individually. Also, one must keep in mind that numerical errors may start creeping in if the sum is extremely large.

## V. ANALYTICAL RESULTS

Instead of calculating  $F(w)$  according to the procedures detailed in Sections III and IV, some symmetric lenses also have analytic expressions for  $F(w)$  which are much more efficient to compute. Here, we provide an overview of the analytic expressions for the amplification factors of two common lens models: point lens and singular isothermal sphere.

### A. Point lens

The amplification factor (13) can be computed analytically for the point-mass lens [17]

$$F_{\text{PL}}(w) = u^{i u} e^{(\pi/2 - 2i t_{\min}) u} \Gamma(1 - i u) {}_1F_1(i u, 1, i u y^2), \quad (55)$$

where  $u = w/2$  and  $t_{\min} = (x_{\min} - y)^2/2 - \log(x_{\min})$  and  $x_{\min} = (y + \sqrt{y^2 + 4})/2$ . The numerical evaluation of the hypergeometric function  ${}_1F_1(a, b, z)$  with complex parameters is costly and it usually requires the use of arbitrary-precision software. However, for the particular case  ${}_1F_1(z, 1, cz)$ , we managed to implement a very fast version based on four different approximations:

- I) *Large c.* We use the asymptotic formula in chapter 27 of [52]. For our precision requirements, we compute it to third order.
- II) *Small c, large z.* Standard asymptotic formula for large argument [53, (13.7.2)].
- III) *Small c, intermediate z.* We first compute the hypergeometric function  ${}_1F_1(z, b, cz)$  for sufficiently large  $b > 1$  using the series expansion [53, (13.2.2)] and then apply the recurrence relation [53, (13.3.2)] to compute the case  $b = 1$ .
- IV) *Small c, small z.* Standard series expansion [53, (13.2.2)].

In our code, we calibrated the switches between different approximations to achieve a given level of precision,



comparing with the arbitrary-precision implementation in ARB<sup>6</sup> [54]. We also provide a slower Python implementation based on mpmath<sup>7</sup> [55]. Fig. 10 shows the level of agreement between both implementations, highlighting the four regions in parameter space where the previous approximations have been used.

### B. Singular isothermal sphere

The lensing potential for the singular isothermal sphere (SIS) is

$$\psi(\mathbf{x}) = \psi_0 |\mathbf{x}| \equiv \psi_0 x . \quad (56)$$

This lens is simple enough that all the geometric optics properties can be computed analytically. The minimum of the Fermat potential is located at  $\mathbf{x} = (y + \psi_0, 0)$  with time delay and magnification given by

$$t_{\min} = \frac{1}{2} \psi_0 (2y + \psi_0) , \quad (57)$$

$$\mu_{\min} = 1 + \frac{\psi_0}{y} . \quad (58)$$

If  $y < \psi_0$ , there is a second critical point, a saddle point, at  $\mathbf{x} = (y - \psi_0, 0)$ . The time delay and magnification at the saddle point are

$$t_{\text{saddle}} = \frac{1}{2} \psi_0 (2y - \psi_0) , \quad (59)$$

$$\mu_{\text{saddle}} = \left| 1 - \frac{\psi_0}{y} \right| . \quad (60)$$

In addition to this, there is a cusp at the origin. It is also possible to compute the full time-domain amplification factor analytically, as we did for the first time in [41]. Instead of  $\psi_0$  and  $y$ , we will express the integral as a function of two new variables,  $u$  and  $R$ ,

$$u \equiv \frac{\sqrt{2\tau}}{\psi_0 + y} , \quad R \equiv \frac{\psi_0 - y}{\psi_0 + y} . \quad (61)$$

The variable  $u$  is a redefined time parameter while  $R$  is a constant, ranging between  $-1$  and  $1$ . The final result can be compactly expressed as

$$I_{\text{SIS}}(\tau) = \frac{8(b-c)}{\sqrt{(a-c)(b-d)}} \left[ \Pi \left( \frac{a-b}{a-c}, r \right) + \frac{cK(r)}{(b-c)} \right] , \quad (62)$$

with

$$r \equiv \sqrt{\frac{(a-b)(c-d)}{(a-c)(b-d)}} , \quad (63)$$

and where  $\Pi$  and  $K$  are, respectively, the complete elliptic integrals of the third and first kind, see e.g. [56]. The coefficients  $a$ ,  $b$ ,  $c$  and  $d$  are functions of the variables  $u$  and  $R$  defined in (61) above. We must however distinguish between three regions

- *Region 1:* ( $u > 1$ )

$$\begin{aligned} a &= 1 + u , & c &= 1 - u , \\ b &= R + \sqrt{u^2 + R^2 - 1} , & d &= R - \sqrt{u^2 + R^2 - 1} . \end{aligned}$$

- *Region 2:* ( $\sqrt{1-R^2} < u < 1$ )

– *Case A:* ( $R > 0$ )

$$\begin{aligned} a &= 1 , & c &= \sqrt{1-u^2} , \\ b &= R , & d &= -\sqrt{1-u^2} . \end{aligned}$$

– *Case B:* ( $R < 0$ )

$$\begin{aligned} a &= 1 , & c &= -\sqrt{1-u^2} , \\ b &= \sqrt{1-u^2} , & d &= R . \end{aligned}$$

- *Region 3:* ( $0 < u < \sqrt{1-R^2}$ )

$$\begin{aligned} a &= 1 , & c &= R , \\ b &= \sqrt{1-u^2} , & d &= -\sqrt{1-u^2} . \end{aligned}$$

The amplification factor in the frequency domain can be also reduced to a simple form, very well suited for numerical computations. First, we can rewrite it as

$$\begin{aligned} F_{\text{SIS}}(w) &= \frac{w}{2\pi i} \int d^2x e^{i w \phi(\mathbf{x})} \\ &= \frac{w e^{i w y^2/2}}{2\pi i} \int_{-\pi}^{\pi} d\theta \int_0^{\infty} r dr e^{i w r(r/2 - y \cos \theta - \psi_0)} . \end{aligned} \quad (64)$$

The radial integral can be expressed in terms of Fresnel integrals [53, (7.2)], and the final expression is

$$F_{\text{SIS}}(w) = e^{i w y^2/2} \left\{ 1 + \int_0^{\pi} d\theta \alpha(\theta) \left( f(-\alpha) - i g(-\alpha) \right) \right\} , \quad (65)$$

where

$$\alpha(\theta) \equiv \sqrt{\frac{w}{\pi}} (\psi_0 + y \cos \theta) . \quad (66)$$

We implemented the Fresnel integrals following the simple prescription given in [57], which achieve an accuracy of  $10^{-8}$ , more than enough for our applications.

<sup>6</sup> <https://github.com/flintlib/arb>

<sup>7</sup> <https://github.com/mpmath/mpmath>

## VI. CODE STRUCTURE AND PERFORMANCE

### A. Outline

GLOW's main goal is to compute the amplification factor starting from a given lens configuration. Our intention when building GLOW was to create a code that is, first and foremost, fast and supports generic lens configurations. To achieve this goal, we developed new methods, explained in the preceding sections, and implemented them in a C library. Furthermore, we wanted to have a modular code that was easy to use by the end user. We have achieved this by developing a Cython wrapper for this library, so that the code can be used entirely from Python. In addition, we also provide a full Python implementation of many of the methods present in the library, although not for all methods, and those that are implemented are not nearly as powerful. Finally, we have a very limited number of external dependencies. The main one is the GNU Scientific Library (GSL)<sup>8</sup> [58], that can be readily installed from public repositories. We also make use of `pocketfft`<sup>9</sup>, that is included in the source files. The code is organized as shown in Fig. 3.

The logic behind the code structure is very simple. There are three main Python modules that must be used in succession and create three objects:  $\text{Lens} \rightarrow I(\tau) \rightarrow F(w)$ . A simple GLOW session looks like this:

```
import numpy as np
from glow.lenses import Psi_SIS
from glow.time_domain_c import It_SingleIntegral_C
from glow.freq_domain_c import Fw_FFT_C

Psi = Psi_SIS()
It = It_SingleIntegral_C(Psi, y=0.3)
Fw = Fw_FFT_C(It)

# computation done, we can evaluate now
ws = np.geomspace(1e-2, 1e2, 1000)
Fws = Fw(ws)
```

The steps in the computation for a typical work session can be summarized as follows:

- I) *Choose a lens.* The lens can be chosen from the comprehensive catalog in App. A, or constructed as the combination of any of these lenses. The lenses are implemented in Python and C, with a script in place to check that the implementations are consistent. In the documentation we provide a guide to implement a new lens model.
- II) *Compute  $I(\tau)$ .* After defining the lens and the impact parameter  $y$ , we can choose the appropriate method to compute the time-domain integral. By

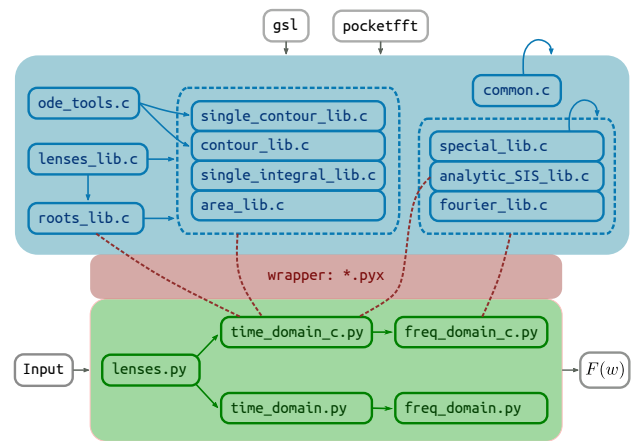


FIG. 3. GLOW's structure. GLOW's core is a standalone C library that is interfaced with a Python frontend through a Cython wrapper. Once the library and the wrapper are compiled, the user only needs basic Python knowledge to operate the code. We also provide additional Python utilities to lens waveforms and to transform between physical units and lensing dimensionless units, as well as tutorials and an online documentation.

default, it will be precomputed on a grid when we initialize the object and any further calls will evaluate an interpolation function.

- III) *Compute  $F(w)$ .* Choosing again from the different methods, we can compute the amplification factor in the frequency domain from the time domain version. Upon initialization, the method shown in the example precomputes  $F(w)$  in a frequency grid, and the evaluation is performed using an interpolation function. This is crucial for waveform lensing, where the amplification factor must be evaluated in a large number of points.
- IV) *Transform to physical units and lens the waveform.* In general, there is not a one-to-one correspondence between the physical parameters of the lens and its dimensionless counterpart used in lensing computations. For instance, the computation shown in the example is valid for any values of the lens mass or redshift, but these parameters are only relevant when we want to convert back to physical frequencies. To lens a waveform we must first choose the physical parameters of the lens and the waveform to be lensed. We provide two additional Python modules to facilitate this task, interfacing with `astropy`<sup>10</sup> [59–61] and `pycbc`<sup>11</sup> [62, 63]. This allows GLOW to directly compute lensed waveforms (in time and frequency domain) starting from generic lenses. See Fig. 5 for an example.

<sup>8</sup> <https://www.gnu.org/software/gsl/>

<sup>9</sup> <https://gitlab.mpcdf.mpg.de/mtr/pocketfft>

<sup>10</sup> <https://github.com/astropy/astropy>

<sup>11</sup> <https://github.com/gwastro/pycbc>

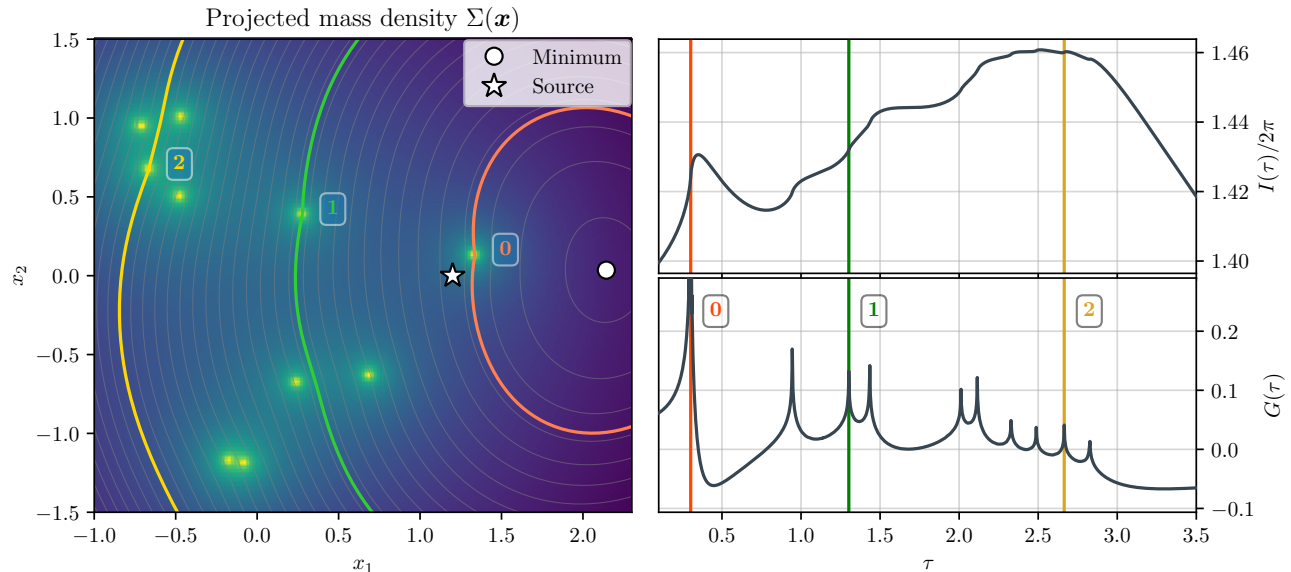


FIG. 4. Example of a non-trivial weak lensing scenario, with 10 SISs. The central cusp of the SIS produces small deformations in the time-domain integral. Even more dramatic is their effect in the Green function,  $G(\tau) \equiv dI/d\tau/2\pi$ , where each lens produces a distinct peak. We highlighted three of them, together with the contour that passes through the center of the lens.

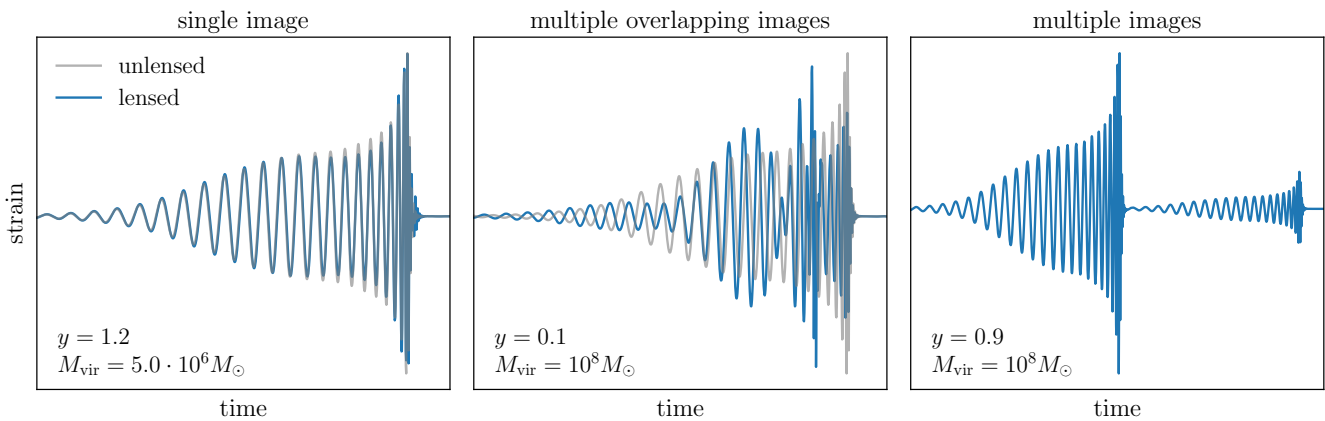


FIG. 5. Example of time-domain GW waveforms. Blue curves represent the lensed waveform, while the unlensed signal is plotted in grey. Here, we considered an equal-mass non-spinning BBH with  $M_{\text{BBH}} = 100 M_{\odot}$ ,  $z_S = 0.3$  and lensed by an SIS lens at  $z_L = 0.15$ . Notice that all the lensed waveforms are produced using GLoW’s analytic SIS implementation of the full wave-optics amplification factor. In this regard, we would like to emphasize that we recover remarkably well what is expected in the GO limit *without* using any GO approximation.

In the remainder of this Section we will review how the methods discussed in Sec. III and IV are implemented in GLoW, focusing on the C version, as well as the code’s performance.

## B. Time domain

The time domain module contains five different methods to compute  $I(\tau)$ :

- **MultiContour.** This class implements the contour

method, outlined in Sec. III A, in full generality. It can handle non-axisymmetric lenses with one or multiple images. See Fig. 6 for an application.

- **SingleContour.** This class also implements the contour method, but only in the single-image regime. Whenever possible, it uses the angular integration (26), that allows for a faster computation in simple scenarios. This class should be preferred over MultiContour for weak lensing computations. A complex example is shown in Fig. 4.
- **SingleIntegral.** Implementation of the method

outlined in Sec. III B. It only supports axisymmetric lenses, with one or multiple images. It is by far the fastest and most reliable method for symmetric lenses. It should be always used over the previous methods when dealing with symmetric lenses.

- **AreaIntegral**. This class implements the method explained in Sec. III C. It supports arbitrary lenses with multiple images. However, the algorithm is very naive and the implementation is not optimized. Its main purpose in the code is to provide an independent cross-check for the other methods. In contrast with all the other methods, it does not require the precomputation of the critical points of the Fermat potential, only the global minimum needs to be found. This method should be avoided for anything beyond cross-checking.
- **AnalyticSIS**. Implementation of (62).

### C. Frequency domain

The frequency domain module contains four different methods to compute  $F(w)$ :

- **FFT**. Computation of the amplification factor using a Fast Fourier Transform (FFT). The implementation follows the scheme outlined in Sec. IV B. It is the fastest way to compute  $F(w)$  for a generic lens. Keep in mind that depending on the input, i.e. lens parameters or frequencies requested, some precision parameters may need to be tuned to achieve optimal results.
- **DirectFT**. Implementation of the Fourier sum presented in IV C. Since we precompute  $I(\tau)$  on a grid and then approximate it by a linear interpolation function (by default, but can be changed), this algorithm returns the exact Fourier transform. Its main disadvantage with respect to FFT is that each frequency  $w$  must be computed individually, making this method usually slower. A clear advantage of this method is that the errors arise only from the insufficient sampling of  $I(\tau)$ , which can be easily improved. This class can be used for highly precise tasks, without high speed requirements, and as a cross-check of FFT.
- **SemiAnalyticSIS**. Implementation of (65).
- **AnalyticPointLens**. Implementation of the analytical formula for the point lens, following the approximations of Sec. V A.

### D. Performance and precision

In this section we will present some tests of the code. All of them have been performed in a laptop with an

$I(\tau)$ method	$y = 0.3$	$y = 1.2$
<b>SingleContour</b>	—	5.5 ms
<b>MultiContour</b>	16 ms	13 ms
<b>SingleIntegral</b>	490 $\mu$ s	480 $\mu$ s
<b>AnalyticSIS</b>	770 $\mu$ s	740 $\mu$ s

TABLE I. Four different computations of the time domain integral for the SIS. The evaluation times correspond to the default initialization time of these objects in the code, which involves computing  $I(\tau)$  on a grid with 5000 points. Notice that the **SingleContour** method can only be used in the single-image regime.

AMD Ryzen 7 8845HS, using 8 threads, and with the default precision parameters.

Table I contains the initialization times for an SIS lens, using different methods in the time domain, both in the strong and the weak lensing regime. Tables II and III show the initialization time for the amplification factor, for  $y = 0.3$  and  $y = 1.2$  respectively. We also include the evaluation time for the analytical point lens, using our improved implementation. The tables' three columns represent:

1. Initialization time of  $F(w)$ , given a time-domain version  $I(\tau)$ .
2. Evaluation time on a frequency grid with 1000 points.
3. Total time including the initialization of  $I(\tau)$ . The analytical expressions do not require  $I(\tau)$  and their initialization time is negligible.

For the precision tests, we compared our new numerical methods with the analytical expressions available for the SIS and the point lens. We check the precision of  $I(\tau)$  for the SIS in Fig. 7, and for the amplification factor we test both the SIS in Fig. 8 and the point lens in 9. The default precision parameters are chosen to target a (relative) tolerance of  $10^{-4}$  for  $I(\tau)$  and  $10^{-3}$  for  $F(w)$ , after interpolation. We also show an example with a tolerance of  $10^{-8}$  with non-default precision parameters. Finally, in Fig. 10 we compare our, extremely fast, implementation of the analytical amplification factor for the point lens with a naive implementation using arbitrary precision. The switches between the different approximations discussed in Sec. V A are calibrated to never exceed a relative error of  $10^{-5}$ .

## VII. CONCLUSIONS

Advances in astronomy may soon enable the detection of wave-optics gravitational lensing phenomena, in which the undulatory nature of the signal becomes manifest. Here we have presented numerical methods capable of studying wave-optics lensing phenomena for lenses representing generic matter distributions. After

$F(w)$ method	Initialization	Eval. $w$	Total
FFT	1.3 ms	43 $\mu$ s	< 17 ms
DirectFT	63 $\mu$ s	4.8 ms	< 21 ms
SemiAnalyticSIS	————	560 $\mu$ s	560 $\mu$ s
AnalyticPointLens	————	77 $\mu$ s	77 $\mu$ s

TABLE II. Computation of the amplification factor for  $y = 0.3$ , for the SIS (first three rows) and point lens (last row). The total time includes the initialization of  $I(\tau)$  in Table I, and we take the slowest method (`MultiContour`) as an upper limit. For symmetric lenses it would be more appropriate to use `SingleIntegral`, which would yield a total time of less than 2 ms.

$F(w)$ method	Initialization	Eval. $w$	Total
FFT	1.1 ms	43 $\mu$ s	< 14 ms
DirectFT	46 $\mu$ s	4.8 ms	< 18 ms
SemiAnalyticSIS	————	1.3 ms	1.3 ms
AnalyticPointLens	————	77 $\mu$ s	77 $\mu$ s

TABLE III. Equivalent of Table II, for impact parameter  $y = 1.2$ .

an overview of the formalism, we describe multiple algorithms to compute the time-domain amplification integral, the frequency-domain amplification factor, and efficient analytic methods for simple lenses. These algorithms have been implemented in a companion software package, *Gravitational lensing of Waves (GLOW)*, which is freely available to the scientific community. GLOW renders the computation of predictions robust for complex lenses. The code is also fast enough to run on a laptop and perform parameter estimation without interpolating precomputed results. It can also be used in generating template banks to search for lensed GW signals that may be missed by regular search pipelines.

As a tool, GLOW will enable the investigation of novel lensing phenomena. Wave-optics effects will facilitate testing and characterizing dark-matter structures. GWs detected by current and future facilities will provide stringent constraints on objects above  $M \gtrsim 100M_{\odot}$  [46, 48, 64–67]. Detection of wave-optics lensing signatures seems promising for LISA [40, 41], especially in the presence of a background lens and for dense dark-matter halos [23]. Pulsar-timing arrays hold the promise to detect wave-optics features by galactic-scale lenses, which may enable a detection of the universe’s expansion rate [24]. Similarly, the high-frequency of electromagnetic observations will allow them to probe sub-solar objects, including planets, primordial black holes and compact dark-matter structures [13, 15, 16]. These studies have been largely based on symmetric lenses: GLOW’s flexibility to incorporate new lens profiles and tackle complex configurations will greatly contribute to this program.

Future developments will expand the capabilities of GLOW. In the near future, we will expand the catalog

of lenses, including non-parametric profiles. To access increasingly realistic scenarios, we will integrate GLOW with publicly available lensing codes like `lenstronomy`<sup>12</sup> [68, 69] or `glafic`<sup>13</sup> [70]. To describe wave-optics lensing by the dense stellar fields in lens galaxies (microlensing) [19–21], we will further optimize and extend our algorithms to account for large number of lenses. To describe collective lensing effects, we will develop multi-plane lensing and ray-tracing in the wave-optics regime [71]. Finally, extensions to GLOW can address scenarios of new physics, such as tests of general relativity [72–74] or time-dependent dark-matter backgrounds [75].

## ACKNOWLEDGMENTS

We are very grateful to G. Brando, P. Mehta, N. Menadeo, J. Raynaud, S. Singh, D. Yushchenko for their feedback on early versions of the code. We also thank E. Berti, M. Caliskan, M. Cheung, S. Delos, JM Ezquiaga, D. Jow, R. Lo, A. Kumar Mehta, A. Mishra, K. Ng, X. Shan, S. Vegetti, Y. Wang for discussions along the way. Besides the libraries mentioned in the main text, GLOW also relies on Numpy [76], Scipy [77] and Colossus<sup>14</sup> [78]. LC was supported by the Princeton German Department’s Summer Work Program. HVR is supported by the Spanish Ministry of Universities through a Margarita Salas Fellowship, with funding from the European Union under the NextGenerationEU programme.

<sup>12</sup> <https://github.com/lenstronomy/lenstronomy>

<sup>13</sup> <https://github.com/oguri/glafic2>

<sup>14</sup> <https://bitbucket.org/bdiemer/colossus/src/master/>



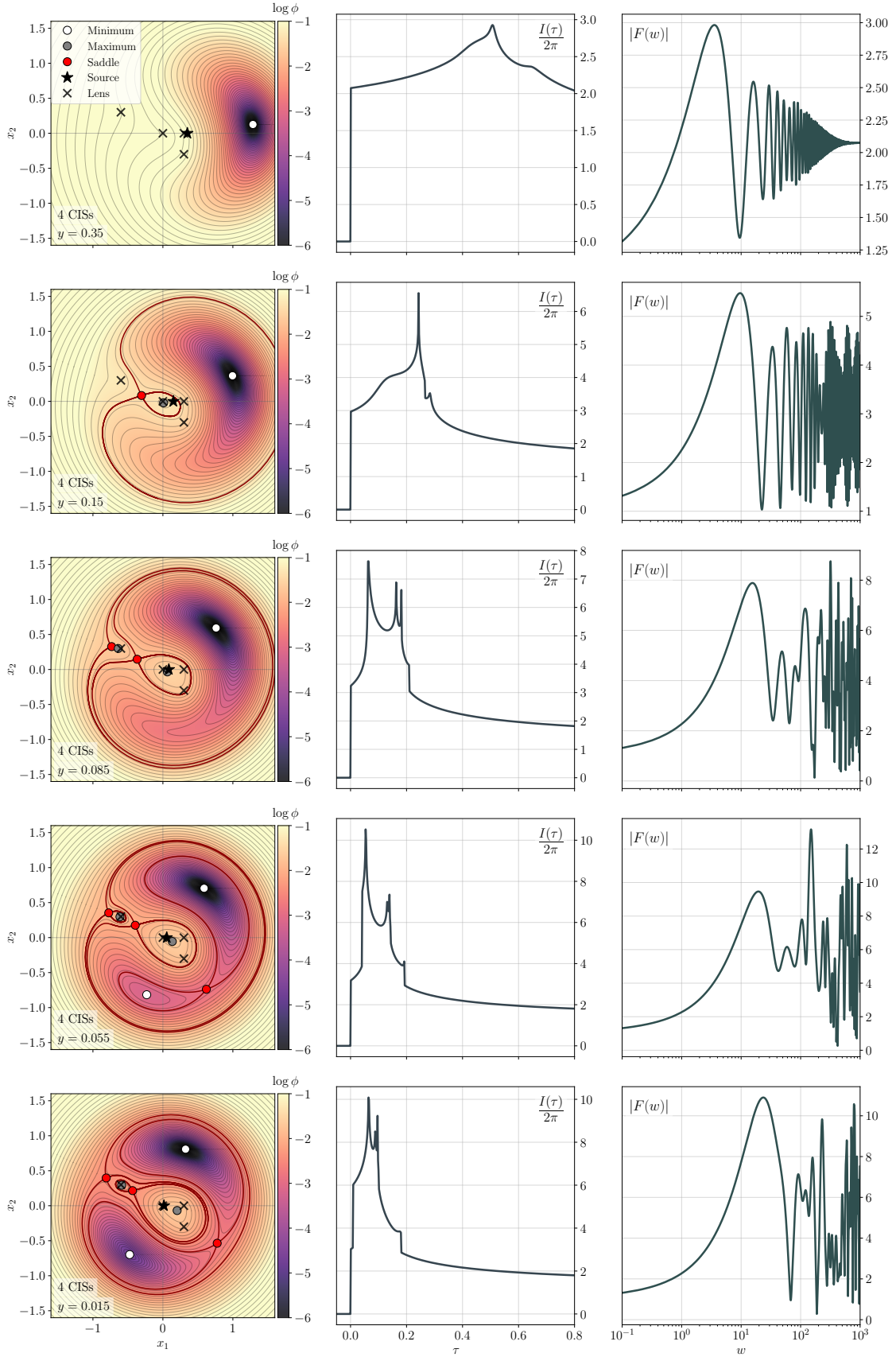


FIG. 6. Example of different non-trivial strong lensing configurations. The lens is fixed, a composite lens with four CISs, and the impact parameter is progressively reduced, from top to bottom. The configuration in the lowest panel corresponds to Fig. 1. The two lower panels ( $y = 0.055$  and  $y = 0.015$ ) illustrate how two configurations with the same number of critical points can have a different saddle point structure.

## Appendix A: Lens catalog

In this Appendix, we will provide a detailed catalog of lens models implemented in `GLoW`. For each lens, we provide its defining density  $\rho(\mathbf{r})$ , projected density  $\Sigma(\boldsymbol{\xi})$  (obtained using Eq. (5)) and expression for the lensing potential  $\psi(\mathbf{x})$  (obtained solving Eq. (6)). As in the main text, in the following we define  $x \equiv |\mathbf{x}|$ .

### 1. Point lens (PL)

The *PL* model is defined by a particle of mass  $M$  localized in a point and resulting in an axially symmetric lensing potential. Its density and projected density are

$$\rho(\mathbf{r}) = M\delta^3(\mathbf{r}), \quad (\text{A1a})$$

$$\Sigma(\boldsymbol{\xi}) = M\delta^2(\boldsymbol{\xi}). \quad (\text{A1b})$$

Defining the Einstein radius as

$$R_E \equiv \sqrt{4GM(1+z_L)d_{\text{eff}}}, \quad (\text{A2})$$

we can write the lensing potential as

$$\psi(x) = \psi_0 \log x, \quad \psi_0 \equiv \frac{R_E^2}{\xi_0^2}. \quad (\text{A3})$$

In this lens model, the so-far unspecified scale  $\xi_0$  can be conveniently fixed by setting  $\psi_0 = 1$ . Note that with this choice the redshifted effective lens mass  $M_{Lz}$ , defined in Eq. (15), coincides with the redshifted mass,  $M_{Lz} = M(1+z_L)$ .

### 2. Singular Isothermal Sphere (SIS)

The *SIS* is a spherically symmetric lens model, defined by a density decaying as an inverse square power of the radial distance, that is typically used to describe halo profiles. The density and projected density are therefore given by

$$\rho(r) = \frac{\sigma_v^2}{2\pi G r^2}, \quad (\text{A4a})$$

$$\Sigma(\xi) = \frac{\sigma_v^2}{2G\xi}, \quad (\text{A4b})$$

where the parameter  $\sigma_v$  is the velocity dispersion of the halo. The lensing potential takes the following simple form

$$\psi(x) = \psi_0 x, \quad \psi_0 \equiv \frac{\sigma_v^2}{G\Sigma_{\text{cr}}\xi_0}. \quad (\text{A5})$$

In this lens model a useful choice for the scale  $\xi_0$  is then  $\xi_0 = \sqrt{4GM_{Lz}d_{\text{eff}}} \equiv \sigma_v^2/(G\Sigma_{\text{cr}})$ , such that  $\psi_0 = 1$ . See e.g. [23, 41] for additional details.

### 3. Cored isothermal sphere (CIS)

The *CIS* lens is a deformation of the *SIS*, where the density smoothens at the lens's centre thanks to the presence of a core of radius  $r_c$ . It is defined as [79, 80]

$$\rho(r) = \rho_0 \frac{r_c^2}{r^2 + r_c^2}, \quad (\text{A6a})$$

$$\Sigma(\xi) = \frac{\pi\rho_0 r_c^2}{\sqrt{\xi^2 + r_c^2}}. \quad (\text{A6b})$$

Here  $\rho_0$  is the central density of the profile. The lensing potential is then obtained as

$$\psi(x) = \psi_0 \sqrt{x^2 + x^2} + x_c \psi_0 \log \left( \frac{2x_c}{\sqrt{x_c^2 + x^2} + x_c} \right), \quad (\text{A7a})$$

$$\psi_0 \equiv \frac{2\pi\rho_0 r_c^2}{\Sigma_{\text{cr}}\xi_0}, \quad (\text{A7b})$$

$$x_c \equiv \frac{r_c}{\xi_0}. \quad (\text{A7c})$$

The parameter  $x_c$  represents a dimensionless core radius and depends on the normalization scale  $\xi_0$ . The latter quantity can be conveniently fixed by setting  $\psi_0 = 1$ , as in the previous lens models. This translates into  $\xi_0 = 2\pi\rho_0 r_c^2/\Sigma_{\text{cr}}$ . Additional details are given for instance in [41, 48].

### 4. Truncated singular isothermal sphere (tSIS)

The mass enclosed by an *SIS* profile is logarithmically divergent, given the  $\sim 1/r^2$  decay of the density. A truncation of the profile at large radii is then needed. In the *tSIS* lens, the density is truncated at a radius  $R$  with a Gaussian cutoff:

$$\rho(r) = \frac{M_{\text{tot}}}{2\pi^{3/2}R^3} \left( \frac{r}{R} \right)^{-2} e^{-r^2/R^2}, \quad (\text{A8a})$$

$$\Sigma(\xi) = \frac{M_{\text{tot}}}{2\pi^{1/2}R^2} \frac{R}{\xi} \text{erfc}(\xi/R). \quad (\text{A8b})$$

Here,  $M_{\text{tot}}$  is the total mass of the profile and  $\text{erfc}(z)$  is the complementary error function. The lensing potential admits an analytic expression as follows:

$$\psi(x) = \psi_0 x \left\{ \frac{1}{2u\sqrt{\pi}} [2\log(u) + E_1(u^2) + \gamma_E] + \text{erfc}(u) + \frac{1 - e^{-u^2}}{u\sqrt{\pi}} \right\}, \quad (\text{A9a})$$

$$u \equiv x\xi_0/R, \quad (\text{A9b})$$

$$\psi_0 \equiv \frac{M_{\text{tot}}}{\sqrt{\pi}\Sigma_{\text{cr}}R\xi_0}, \quad (\text{A9c})$$

where  $E_1(z)$  is the exponential integral and  $\gamma_E$  is the Euler-Mascheroni constant. Again, the most convenient choice for the scale  $\xi_0$  is obtained by setting  $\psi_0 = 1$ .

## 5. Elliptical Singular Isothermal Sphere (eSIS)

The following lens is a phenomenological model for a potential with elliptical symmetry. For simplicity, we added the ellipticity in the lensing potential, rather than the mass density. See [81] and references therein for more details on elliptical lens profiles. This lens, that we have (somewhat paradoxically) dubbed elliptical SIS, *eSIS*, is a specific example of the softened power law potential in [81]. The lensing potential is

$$\psi(\mathbf{x}) = \psi_0 \sqrt{x_1^2 + x_2^2/q^2}, \quad \psi_0 \equiv \frac{\sigma_v^2}{G \Sigma_{\text{cr}} \xi_0}, \quad (\text{A10})$$

where  $q$  controls the ellipticity of the profile. Different choices for the orientation of the semi-major axis are implemented through a rotation of angle  $\alpha$  in the lens plane

$$x'_1 = \cos \alpha x_1 - \sin \alpha x_2, \quad (\text{A11a})$$

$$x'_2 = \sin \alpha x_1 + \cos \alpha x_2. \quad (\text{A11b})$$

The lensing potential in this more general setting is then given by  $\psi_\alpha(\mathbf{x}) = \psi(x'_1, x'_2)$ .

## 6. Navarro-Frenk-White (NFW)

The *NFW* is the most commonly used spherically symmetric profile to model cold dark-matter halos [82] and is defined by the following  $\rho(r)$  and  $\Sigma(\xi)$

$$\rho(r) = \frac{\rho_s}{(r/r_s)(1+r/r_s)^2}, \quad (\text{A12a})$$

$$\Sigma(\xi) = 2\rho_s r_s \frac{1 - \mathcal{F}(\xi/r_s)}{(\xi/r_s)^2 - 1}, \quad (\text{A12b})$$

where

$$\mathcal{F}(x) \equiv \begin{cases} \frac{1}{\sqrt{x^2-1}} \arctan(\sqrt{x^2-1}), & x > 1 \\ \frac{1}{\sqrt{1-x^2}} \operatorname{arctanh}(\sqrt{1-x^2}). & x < 1 \end{cases} \quad (\text{A13})$$

The parameter  $r_s$  is the so-called scale radius while  $\rho_s/4$  is the density at  $r_s$ . Solving the projected Poisson's equation one finds the following form for the lensing potential

$$\psi(x) = \frac{1}{2} \psi_0 [\log^2(u/2) + (u^2 - 1)\mathcal{F}^2(u)], \quad (\text{A14a})$$

$$u \equiv x \xi_0 / r_s, \quad (\text{A14b})$$

$$\psi_0 \equiv \frac{4\rho_s r_s^3}{\Sigma_{\text{cr}} \xi_0^2}. \quad (\text{A14c})$$

As for the lens models discussed previously, a convenient choice is to set  $\psi_0 = 1$ . However, different normalization choices are often adopted in lensing applications (see e.g. [67, 83, 84]).

## 7. External Shear and Convergence

The external effects due to a galaxy or cluster can be represented by constant convergence and shear. This is particularly useful for embedding small-scale lenses like stars or black holes within a galaxy [20]

$$\psi(x_1, x_2) = \frac{\kappa}{2}(x_1^2 + x_2^2) + \frac{\gamma_1}{2}(x_1^2 - x_2^2) + \gamma_2 x_1 x_2. \quad (\text{A15})$$

In the above lensing potential, the parameter  $\kappa$  is the convergence while  $\gamma_1$  and  $\gamma_2$  are shear components along  $x_1$  and  $x_2$  respectively.

## Appendix B: Regularization scheme

The regularizing functions used in (50) are defined as

$$R_0(\alpha, \beta, \sigma; x) \equiv \frac{\beta \Theta(x)}{(x^2 + (\beta/\alpha)^{2/\sigma})^{\sigma/2}}, \quad (\text{B1})$$

$$R_1(\alpha, \beta, \sigma; x) \equiv x R_0(\alpha, \beta, \sigma + 1; x), \quad (\text{B2})$$

$$R_L(\alpha, \beta; x) \equiv R_1(\alpha, \beta, 1; x) = \frac{\beta x \Theta(x)}{x^2 + \beta/\alpha}, \quad (\text{B3})$$

$$S(A, B; x) \equiv \frac{AB}{2} \Theta(x) \log \left| \frac{B+x}{B-x} \right|, \quad (\text{B4})$$

$$S_{\text{full}}(A, B; x) \equiv S(A, B; x) - R_L(A, AB^2; x). \quad (\text{B5})$$

Their frequency-domain versions are defined as

$$\tilde{R}(w) \equiv -iw \int_{-\infty}^{\infty} e^{iw\tau} R(\tau) d\tau, \quad (\text{B6})$$

All of them are analytical, and the integrals needed can be found in [56],

$$\tilde{R}_0(\alpha, \beta, \sigma; w) = \sqrt{\pi}\alpha\Gamma\left(1 - \frac{\sigma}{2}\right) \left\{ \frac{2}{\pi} \left(\frac{wC_0}{2}\right)^{\frac{1+\sigma}{2}} e^{-i\frac{\pi\sigma}{2}} K_{\frac{1-\sigma}{2}}(wC_0) - \left(\frac{wC_0}{2}\right) \tilde{\mathbb{M}}_{\frac{1-\sigma}{2}}(wC_0) \right\}, \quad (\text{B7})$$

$$\begin{aligned} \tilde{R}_1(\alpha, \beta, \sigma; w) &= \frac{2\alpha C_1}{\sqrt{\pi}} \left(\frac{wC_1}{2}\right)^{1+\frac{\sigma}{2}} e^{-i\frac{\pi\sigma}{2}} \Gamma\left(\frac{1-\sigma}{2}\right) K_{1-\frac{\sigma}{2}}(wC_1) \\ &\quad + \frac{i\alpha C_1}{1-\sigma} wC_1 \left\{ 1 + \sqrt{\pi}\Gamma\left(\frac{3-\sigma}{2}\right) \left(\frac{wC_1}{2}\right) \tilde{\mathbb{M}}_{1-\frac{\sigma}{2}}(wC_1) \right\}, \end{aligned} \quad (\text{B8})$$

$$\tilde{R}_L(\alpha, \beta; w) = \frac{\pi}{2}\beta w e^{-w\sqrt{\beta/\alpha}} + i\beta\frac{w}{2} \left\{ e^{-w\sqrt{\beta/\alpha}} \text{Ei}\left(w\sqrt{\frac{\beta}{\alpha}}\right) - e^{w\sqrt{\beta/\alpha}} E_1\left(w\sqrt{\frac{\beta}{\alpha}}\right) \right\}, \quad (\text{B9})$$

$$\tilde{S}(A, B; w) = -i\frac{\pi}{2}AB e^{iwB} - iAB \left( \cos(wB)\text{si}(wB) - \sin(wB)\text{ci}(wB) \right), \quad (\text{B10})$$

---

with  $C_0 \equiv (\beta/\alpha)^{1/\sigma}$ ,  $C_1 \equiv (\beta/\alpha)^{1/(\sigma+1)}$  and  $\tilde{\mathbb{M}}_\nu(z) \equiv (2/z)^\nu \mathbb{M}_\nu(z)$ . The following special functions have been used:

$K_\nu(z)$  : Irregular modified Bessel function  
[53, (10.25)]

$\mathbb{M}_\nu(z)$  : Modified Struve function  
[53, (11.2.6)]

$E_1(z)$ ,  $\text{Ei}(z)$  : Exponential integrals  
[53, (6.2.1)] and [53, (6.2.5)]

$\text{si}(z)$ ,  $\text{ci}(z)$  : Sine and cosine integrals  
[53, (6.2.10)] and [53, (6.2.11)]

## Appendix C: Code precision

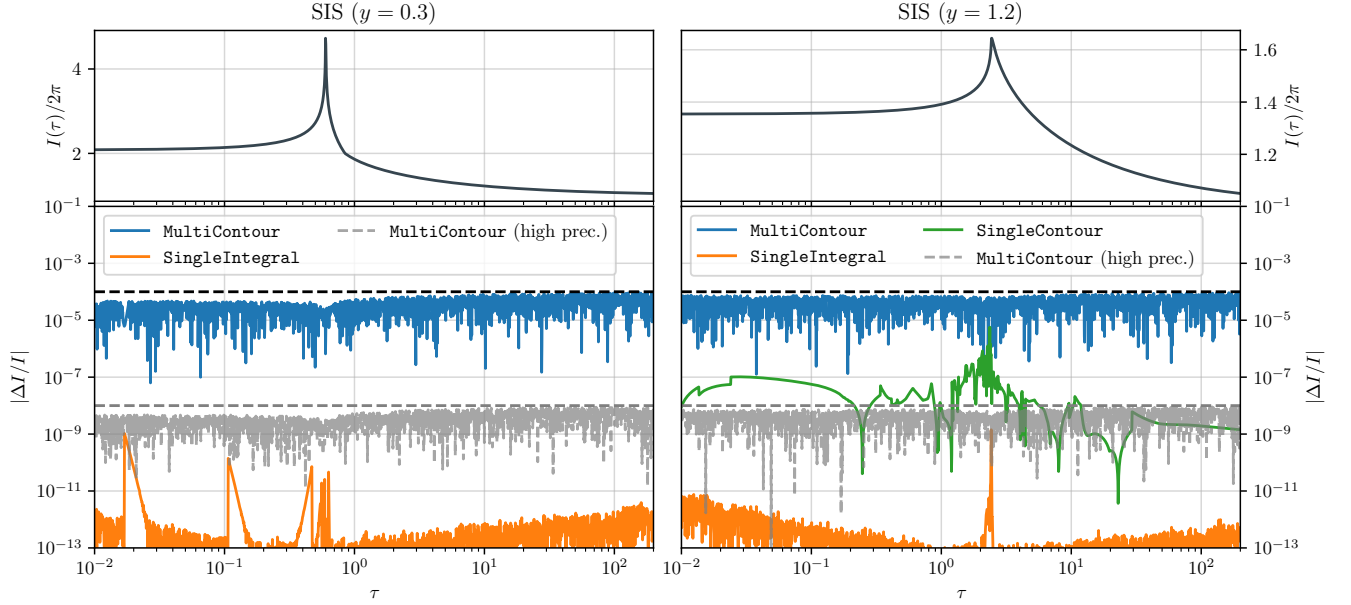


FIG. 7. Time domain integral for the SIS, in the strong and weak lensing regimes. In the lower panel we show the relative difference with respect to the analytical expression (62). In this case, all the points have been computed exactly, i.e. without interpolation. The curve labelled as (high prec.) shows how an appropriate tuning of the precision parameters can easily increase the precision, without a significant impact on the performance. All the other curves use the default precision parameters, chosen to ensure a relative tolerance of  $10^{-4}$ . Note that, due to the simplicity of the SIS potential, the **SingleIntegral** method significantly overperforms in this case.

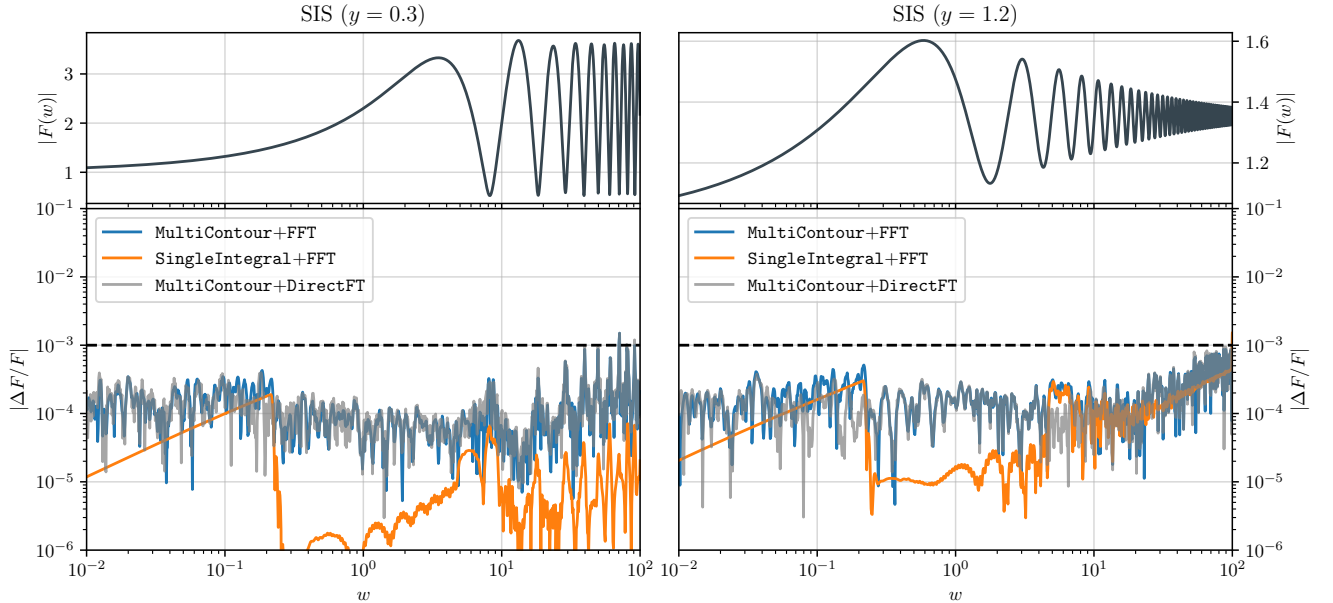


FIG. 8. Amplification factor for the SIS, in the strong and weak lensing regimes. In the lower panel we show the relative difference with respect to the semianalytic expression in (65), using the default parameters in the code. It is important to note that these are the results *after* interpolating  $F(w)$  on a grid, using cubic interpolation. The **MultiContour** results are dominated by the inaccuracies in the computation of the time domain integral, see Fig. 7, while the errors for **SingleIntegral** are dominated by the inaccuracies introduced by the FFT.



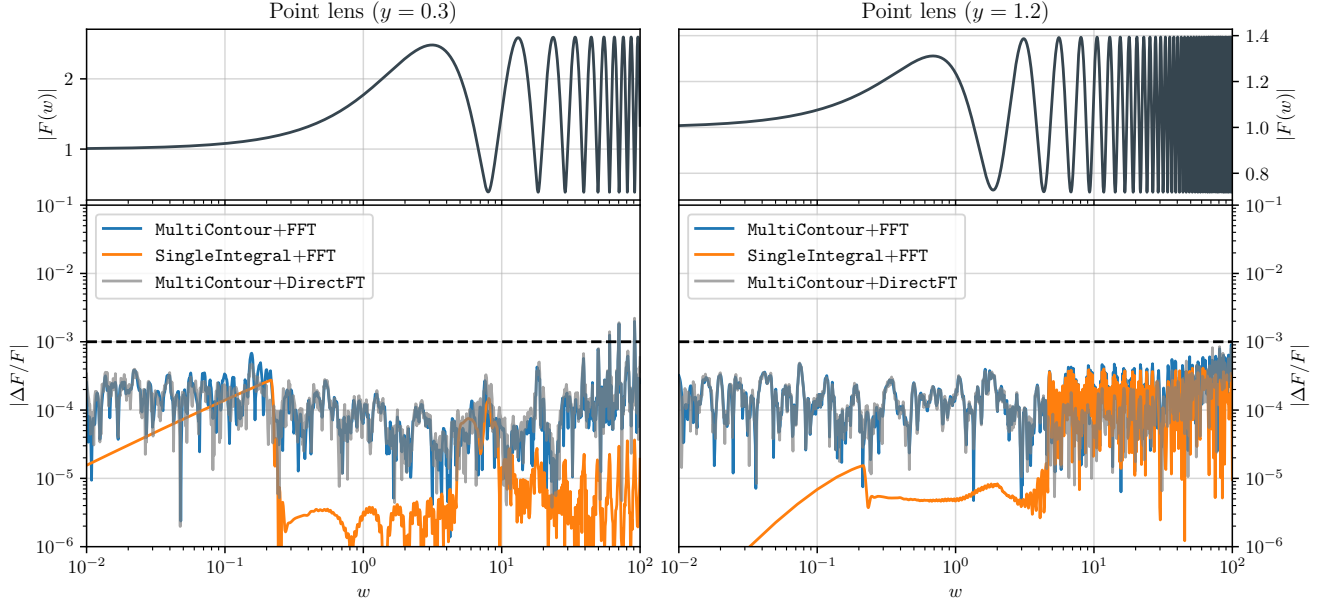


FIG. 9. Amplification factor for the point lens, with two different impact parameters. In the lower panel we show the relative difference with respect to the analytic expression in (55), using the default parameters in the code. It is important to note that this are the results *after* interpolating  $F(w)$  on a grid, using cubic interpolation.

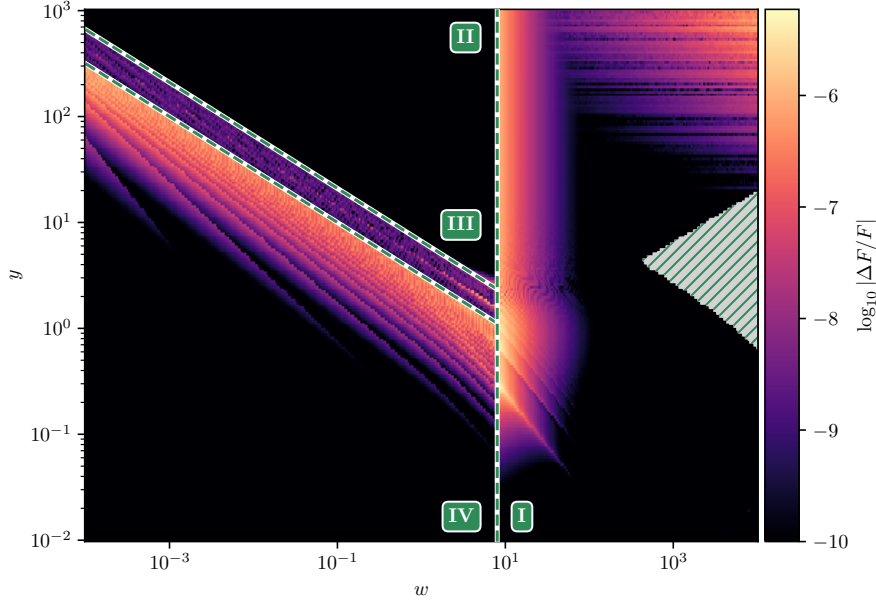


FIG. 10. Relative errors on the analytical point lens implementation. We compare the implementation based on the approximations discussed in Sec. V A (and highlighted in the figure), with a classical implementation using arbitrary precision based on `mpmath` and also available in our code. The switches between the different approximations are calibrated to never exceed a tolerance of  $10^{-5}$ . The maximum difference in this particular grid of  $400 \times 200$  points is  $5 \times 10^{-6}$ . In the hatched region, the computation using arbitrary precision becomes prohibitively expensive. Finally, the errors in the upper right corner arise from numerical errors not in  ${}_1F_1$ , but in the other pieces of the amplification factor. Although  $F(w)$  is essentially 1 in this corner, the geometric optics approximation excels in this region and it can be used to increase the precision further, if needed.

- [1] P. Schneider, J. Ehlers, and E. E. Falco, *Gravitational Lenses*, Astronomy and astrophysics library (Springer, Berlin, Germany, 1999).
- [2] Y. Tsapras, *Geosciences* **8**, 365 (2018), arXiv:1810.02691 [astro-ph.EP].
- [3] B. S. Gaudi *et al.*, *Science* **319**, 927 (2008), arXiv:0802.1920 [astro-ph].
- [4] K. Akiyama *et al.* (Event Horizon Telescope), *Astrophys. J. Lett.* **875**, L1 (2019), arXiv:1906.11238 [astro-ph.GA].
- [5] K. Akiyama *et al.* (Event Horizon Telescope), *Astrophys. J. Lett.* **930**, L12 (2022), arXiv:2311.08680 [astro-ph.HE].
- [6] D. Clowe, M. Bradac, A. H. Gonzalez, M. Markevitch, S. W. Randall, C. Jones, and D. Zaritsky, *Astrophys. J. Lett.* **648**, L109 (2006), arXiv:astro-ph/0608407.
- [7] N. Aghanim *et al.* (Planck), *Astron. Astrophys.* **641**, A8 (2020), arXiv:1807.06210 [astro-ph.CO].
- [8] S. Vegetti *et al.*, *Space Sci. Rev.* **220**, 58 (2024), arXiv:2306.11781 [astro-ph.CO].
- [9] K. C. Wong *et al.* (H0LiCOW), *Mon. Not. Roy. Astron. Soc.* **498**, 1420 (2020), arXiv:1907.04869 [astro-ph.CO].
- [10] R. Reyes, R. Mandelbaum, U. Seljak, T. Baldauf, J. E. Gunn, L. Lombriser, and R. E. Smith, *Nature* **464**, 256 (2010), arXiv:1003.2185 [astro-ph.CO].
- [11] T. E. Collett, L. J. Oldham, R. J. Smith, M. W. Auger, K. B. Westfall, D. Bacon, R. C. Nichol, K. L. Masters, K. Koyama, and R. van den Bosch, *Science* **360**, 1342 (2018), arXiv:1806.08300 [astro-ph.CO].
- [12] C. Leung, D. Jow, P. Saha, L. Dai, M. Oguri, and L. V. E. Koopmans, (2023), arXiv:2304.01202 [astro-ph.HE].
- [13] A. Ulmer and J. Goodman, *Astrophys. J.* **442**, 67 (1995), arXiv:astro-ph/9406042.
- [14] M. Oguri, *Rept. Prog. Phys.* **82**, 126901 (2019), arXiv:1907.06830 [astro-ph.CO].
- [15] D. L. Jow, S. Foreman, U.-L. Pen, and W. Zhu, *Mon. Not. Roy. Astron. Soc.* **497**, 4956 (2020), arXiv:2002.01570 [astro-ph.HE].
- [16] M. Tamta, N. Raj, and P. Sharma, (2024), arXiv:2405.20365 [astro-ph.HE].
- [17] R. Takahashi and T. Nakamura, *Astrophys. J.* **595**, 1039 (2003), arXiv:astro-ph/0305055.
- [18] P. Christian, S. Vitale, and A. Loeb, *Phys. Rev. D* **98**, 103022 (2018), arXiv:1802.02586 [astro-ph.HE].
- [19] J. M. Diego, O. A. Hannuksela, P. L. Kelly, T. Broadhurst, K. Kim, T. G. F. Li, G. F. Smoot, and G. Pagano, *Astron. Astrophys.* **627**, A130 (2019), arXiv:1903.04513 [astro-ph.CO].
- [20] A. Mishra, A. K. Meena, A. More, S. Bose, and J. S. Bagla, *Mon. Not. Roy. Astron. Soc.* **508**, 4869 (2021), arXiv:2102.03946 [astro-ph.CO].
- [21] X. Shan, X. Chen, B. Hu, and R.-G. Cai, (2023), arXiv:2301.06117 [astro-ph.IM].
- [22] M. Çalıřkan, N. Anil Kumar, L. Ji, J. M. Ezquiaga, R. Cotesta, E. Berti, and M. Kamionkowski, *Phys. Rev. D* **108**, 123543 (2023), arXiv:2307.06990 [astro-ph.CO].
- [23] G. Brando, S. Goyal, S. Savastano, H. Villarrubia-Rojo, and M. Zumalacárregui, (2024), arXiv:2407.04052 [gr-qc].
- [24] D. L. Jow and U.-L. Pen, (2024), arXiv:2407.03214 [astro-ph.CO].
- [25] P. Auclair *et al.* (LISA Cosmology Working Group), *Living Rev. Rel.* **26**, 5 (2023), arXiv:2204.05434 [astro-ph.CO].
- [26] R. Takahashi, *Astron. Astrophys.* **423**, 787 (2004), arXiv:astro-ph/0402165.
- [27] L. Dai, S.-S. Li, B. Zackay, S. Mao, and Y. Lu, *Phys. Rev. D* **98**, 104029 (2018), arXiv:1810.00003 [gr-qc].
- [28] A. J. Moylan, D. E. McClelland, S. M. Scott, A. C. Searle, and G. V. Bicknell, in *11th Marcel Grossmann Meeting on General Relativity* (2007) pp. 807–823, arXiv:0710.3140 [gr-qc].
- [29] X. Guo and Y. Lu, *Phys. Rev. D* **102**, 124076 (2020), arXiv:2012.03474 [gr-qc].
- [30] M. H.-Y. Cheung, K. K. Y. Ng, M. Zumalacárregui, and E. Berti, “Probing minihalo lenses with diffracted gravitational waves,” (2024), arXiv:2403.13876 [gr-qc].
- [31] M. H. Y. Cheung, J. Gais, O. A. Hannuksela, and T. G. F. Li, *Mon. Not. Roy. Astron. Soc.* **503**, 3326 (2021), arXiv:2012.07800 [astro-ph.HE].
- [32] S. M. C. Yeung, M. H. Y. Cheung, J. A. J. Gais, O. A. Hannuksela, and T. G. F. Li, *Monthly Notices of the Royal Astronomical Society* (2021), arXiv:2112.07635 [gr-qc].
- [33] G. Grillo and J. Cordes, (2018), arXiv:1810.09058 [astro-ph.CO].
- [34] J. Feldbrugge, U.-L. Pen, and N. Turok, *Annals Phys.* **451**, 169255 (2023), arXiv:1909.04632 [astro-ph.HE].
- [35] D. L. Jow, U.-L. Pen, and J. Feldbrugge, *Mon. Not. Roy. Astron. Soc.* **525**, 2107 (2023), arXiv:2204.12004 [astro-ph.HE].
- [36] P. C. Peters, *Physical Review D* **9**, 2207 (1974).
- [37] N. Matsunaga and K. Yamamoto, *JCAP* **01**, 023 (2006), arXiv:astro-ph/0601701.
- [38] M. Wright and M. Hendry, *The Astrophysical Journal* **935**, 68 (2022).
- [39] Z. Gao, X. Chen, Y.-M. Hu, J.-D. Zhang, and S.-J. Huang, *Mon. Not. Roy. Astron. Soc.* **512**, 1 (2022), arXiv:2102.10295 [astro-ph.CO].
- [40] M. Çalıřkan, L. Ji, R. Cotesta, E. Berti, M. Kamionkowski, and S. Marsat, *Physical Review D* (2022), arXiv:2206.02803 [astro-ph.CO].
- [41] S. Savastano, G. Tambalo, H. Villarrubia-Rojo, and M. Zumalacárregui, *Phys. Rev. D* **108**, 103532 (2023), arXiv:2306.05282 [gr-qc].
- [42] G. Pagano, O. A. Hannuksela, and T. G. F. Li, *Astron. Astrophys.* **643**, A167 (2020), arXiv:2006.12879 [astro-ph.CO].
- [43] X. Shan, G. Li, X. Chen, W. Zheng, and W. Zhao, *Sci. China Phys. Mech. Astron.* **66**, 239511 (2023), arXiv:2208.13566 [astro-ph.CO].
- [44] X. Shan, X. Chen, B. Hu, and G. Li, (2023), arXiv:2306.14796 [astro-ph.CO].
- [45] A. Mishra, A. K. Meena, A. More, and S. Bose, *Monthly Notices of the Royal Astronomical Society* **531**, 764 (2024), <https://academic.oup.com/mnras/article-pdf/531/1/764/57707112/stae836.pdf>.
- [46] M. Zumalacárregui, (2024), arXiv:2404.17405 [gr-qc].
- [47] G. Tambalo, M. Zumalacárregui, L. Dai, and M. H.-Y. Cheung, *Phys. Rev. D* **108**, 043527 (2023), arXiv:2210.05658 [gr-qc].
- [48] G. Tambalo, M. Zumalacárregui, L. Dai, and M. H.-Y. Cheung, *Phys. Rev. D* **108**, 103529 (2023),

- arXiv:2212.11960 [astro-ph.CO].
- [49] M. H.-Y. Cheung, K. K. Y. Ng, M. Zumalacárregui, and E. Berti, *Phys. Rev. D* **109**, 124020 (2024), arXiv:2403.13876 [gr-qc].
- [50] J. M. Diego, *Phys. Rev. D* **101**, 123512 (2020), arXiv:1911.05736 [astro-ph.CO].
- [51] S. M. C. Yeung, M. H. Y. Cheung, E. Seo, J. A. J. Gais, O. A. Hannuksela, and T. G. F. Li, *Mon. Not. Roy. Astron. Soc.* **526**, 2230 (2023), arXiv:2112.07635 [gr-qc].
- [52] N. M. Temme, *Asymptotic methods for integrals*, Series In Analysis (World Scientific Publishing, Singapore, Singapore, 2014).
- [53] DLMF, “*NIST Digital Library of Mathematical Functions*,” <https://dlmf.nist.gov/>, Release 1.1.12 of 2023-12-15 (2023), f. W. J. Olver, A. B. Olde Daalhuis, D. W. Lozier, B. I. Schneider, R. F. Boisvert, C. W. Clark, B. R. Miller, B. V. Saunders, H. S. Cohl, and M. A. McClain, eds.
- [54] F. Johansson, *IEEE Transactions on Computers* **66**, 1281 (2017).
- [55] T. mpmath development team, *mpmath: a Python library for arbitrary-precision floating-point arithmetic (version 1.3.0)* (2023), <http://mpmath.org/>.
- [56] I. S. Gradshteyn and I. M. Ryzhik, *Table of Integrals, Series, and Products* (Academic Press, 2007).
- [57] J. Boersma, *Mathematics of Computation* (1960).
- [58] M. Galassi, J. Davies, J. Theiler, B. Gough, G. Jungman, P. Alken, M. Booth, F. Rossi, and R. Ulerich, *GNU scientific library* (Network Theory Limited Godalming, 2002).
- [59] T. P. Robitaille *et al.* (Astropy), *Astron. Astrophys.* **558**, A33 (2013), arXiv:1307.6212 [astro-ph.IM].
- [60] A. M. Price-Whelan *et al.* (Astropy), *Astron. J.* **156**, 123 (2018), arXiv:1801.02634.
- [61] A. M. Price-Whelan *et al.* (Astropy), *Astrophys. J.* **935**, 167 (2022), arXiv:2206.14220 [astro-ph.IM].
- [62] C. M. Bower, C. D. Capano, S. De, M. Cabero, D. A. Brown, A. H. Nitz, and V. Raymond, *Publ. Astron. Soc. Pac.* **131**, 024503 (2019), arXiv:1807.10312 [astro-ph.IM].
- [63] A. Nitz, I. Harry, D. Brown, C. M. Bower, J. Willis, T. D. Canton, C. Capano, T. Dent, L. Pekowsky, G. S. C. Davies, S. De, M. Cabero, S. Wu, A. R. Williamson, B. Machenschalk, D. Macleod, F. Pannarale, P. Kumar, S. Reyes, and A. Tolley, “gwastro/pycbc: v2.3.3 release of pycbc,” (2024), software.
- [64] M. Oguri and R. Takahashi, *Astrophys. J.* **901**, 58 (2020), arXiv:2007.01936 [astro-ph.CO].
- [65] H. Gil Choi, S. Jung, P. Lu, and V. Takhistov, (2023), arXiv:2311.17829 [astro-ph.CO].
- [66] J. Urrutia and V. Vaskonen, *Mon. Not. Roy. Astron. Soc.* **509**, 1358 (2021), arXiv:2109.03213 [astro-ph.CO].
- [67] M. Fairbairn, J. Urrutia, and V. Vaskonen, *JCAP* **07**, 007 (2023), arXiv:2210.13436 [astro-ph.CO].
- [68] S. Birrer and A. Amara, (2018), 10.1016/j.dark.2018.11.002, arXiv:1803.09746 [astro-ph.CO].
- [69] S. Birrer *et al.*, *J. Open Source Softw.* **6**, 3283 (2021), arXiv:2106.05976 [astro-ph.CO].
- [70] M. Oguri, *Publ. Astron. Soc. Jap.* **62**, 1017 (2010), arXiv:1005.3103 [astro-ph.CO].
- [71] J. Feldbrugge, *Mon. Not. Roy. Astron. Soc.* **520**, 2995 (2023), arXiv:2010.03089 [astro-ph.CO].
- [72] J. M. Ezquiaga and M. Zumalacárregui, *Phys. Rev. D* **102**, 124048 (2020), arXiv:2009.12187 [gr-qc].
- [73] C. Dalang, P. Fleury, and L. Lombriser, *Phys. Rev. D* **103**, 064075 (2021), arXiv:2009.11827 [gr-qc].
- [74] S. Goyal, A. Vijaykumar, J. M. Ezquiaga, and M. Zumalacárregui, *Phys. Rev. D* **108**, 024052 (2023), arXiv:2301.04826 [gr-qc].
- [75] S. Jung, T. Kim, J. Soda, and Y. Urakawa, *Phys. Rev. D* **102**, 055013 (2020), arXiv:2003.02853 [hep-ph].
- [76] C. R. Harris and *et al.*, *Nature* **585**, 357 (2020).
- [77] P. Virtanen and *et al.*, *Nature Methods* **17**, 261 (2020).
- [78] B. Diemer, *Astrophys. J. Suppl.* **239**, 35 (2018), arXiv:1712.04512 [astro-ph.CO].
- [79] G. Hinshaw and L. M. Krauss, *Astrophysical Journal*, Part 1 (ISSN 0004-637X), vol. 320, Sept. 15, 1987, p. 468-476. **320**, 468 (1987).
- [80] R. A. Flores and J. R. Primack, *Astrophys. J. Lett.* **457**, L5 (1996), arXiv:astro-ph/9512063.
- [81] C. R. Keeton, (2001), arXiv:astro-ph/0102341.
- [82] J. F. Navarro, C. S. Frenk, and S. D. M. White, *Astrophys. J.* **490**, 493 (1997), arXiv:astro-ph/9611107.
- [83] X. Guo and Y. Lu, (2022), arXiv:2207.00325 [astro-ph.CO].
- [84] H. G. Choi, C. Park, and S. Jung, *Phys. Rev. D* **104**, 063001 (2021), arXiv:2103.08618 [astro-ph.CO].